WILEY LIMNOLOGY AND OCEANOGRAPHY

Removal of methane though hydrological, microbial, and geochemical processes in the shallow sediments of pockmarks along eastern Vestnesa Ridge (Svalbard)

Journal:	*Limnology and Oceanography*
Manuscript ID	LO-15-0348.R1
Wiley - Manuscript type:	Original Article
Date Submitted by the Author:	n/a
Complete List of Authors:	Hong, Wei-Li; CAGE - Centre for Arctic Gas Hydrate, Environment and Climate, Department of Geology UiT Sauer, Simone; Geological survey of Norway (NGU), Panieri, Giuliana; CAGE - Centre for Arctic Gas Hydrate, Environment and Climate, Department of Geology UiT Ambrose Jr., William; CAGE - Centre for Arctic Gas Hydrate, Environment and Climate, Department of Geology UiT; Department of Biology, Bates College; National Science Foundation, Division of Polar Programs Plaza-Faverola, Andreia; CAGE - Centre for Arctic Gas Hydrate, Environment and Climate, Department of Geology UiT Schneider, Andrea; CAGE - Centre for Arctic Gas Hydrate, Environment and Climate, Department of Geology UiT
Keywords:	methane seep, numerical modeling, anaerobic oxidation of methane
Abstract:	The recent discovery of methane seeps in the Arctic region requires a better understanding of the fate of methane in marine sediments if we are to understand the contributions of methane to Arctic ecosystems and climate change. To further this goal, we analyze pore water data from five pockmarks along eastern Vestnesa Ridge, a sediment drift northwest of Svalbard, to quantify the consumption of dissolved methane in the sediments 3-5 meters below seafloor. We use transport-reaction models to quantify the hydrology as well as the carbon mass balance in the sediments. Pore water profiles and our model results demonstrate that hydrological, microbial, and geochemical processes/reactions efficiently remove methane carbon from fluid over different time scales. We interpret the non-steady-state behavior of the first 50-70 cm of our pore water profiles from the active sites as an annual scale downward fluid flow due to a seepage-related pressure imbalance. Such downward flow dilutes the concentration of methane within this depth range. Our steady-state modeling confirms the efficiency of anaerobic oxidation of methane (AOM) in consuming dissolved methane in the upper 0.8 to 1.2 meter of sediments. Based on the phosphate profiles, we estimate that AOM at the active pockmarks may have been operating for the last two to four centuries. Precipitation of authigenic carbonate removes a significant fraction of methane carbon from fluid. More than a quarter of the dissolved inorganic carbon produced by AOM is fixed as authigenic carbonate in the

	sediments, a process that sequestrates methane carbon over geological time.

Removal of methane though hydrological, microbial, and geochemical processes in the shallow sediments of pockmarks along eastern Vestnesa Ridge (Svalbard)

Wei-Li Hong[1], Simone Sauer[1,2], Giuliana Panieri[1], William G. Ambrose Jr.[1,3,4], Andreia Plaza-Faverola[1], and Andrea Schneider[1]

[1] CAGE - Centre for Arctic Gas Hydrate, Environment and Climate, Department of Geology, UiT The Arctic University of Norway, Tromsø, Norway

[2] Geological Survey of Norway (NGU), Trondheim, Norway

[3] Department of Biology, Bates College, Lewiston, Maine USA 04240

[4] National Science Foundation, Division of Polar Programs, Arlington, Va. 22203

Abstract

The recent discovery of methane seeps in the Arctic region requires a better understanding of the fate of methane in marine sediments if we are to understand the contributions of methane to Arctic ecosystems and climate change. To further this goal, we analyze pore water data from five pockmarks along eastern Vestnesa Ridge, a sediment drift northwest of Svalbard, to quantify the consumption of dissolved methane in the sediments 3-5 meters below seafloor. We use transport-reaction models to quantify the hydrology as well as the carbon mass balance in the sediments. Pore water profiles and our model results demonstrate that hydrological, microbial, and geochemical processes/reactions efficiently remove methane carbon from fluid over different time scales. We interpret the non-steady-state behavior of the first 50-70 cm of our pore water profiles from the active sites as an annual scale downward fluid flow due to a seepage-related pressure imbalance. Such downward flow dilutes the concentration of methane within this depth range. Our steady-state modeling confirms the efficiency of anaerobic oxidation of methane (AOM) in consuming dissolved methane in the upper 0.8 to 1.2 meter of sediments. Based on the phosphate profiles, we estimate that AOM at the active pockmarks may have been operating for the last two to four centuries. Precipitation of authigenic carbonate removes a significant fraction of methane carbon from fluid. More than a quarter of the dissolved inorganic carbon produced by

AOM is fixed as authigenic carbonate in the sediments, a process that sequestrates methane carbon over geological time.

Keywords: methane seep, numerical modeling, anaerobic oxidation of methane

Introduction

Pockmarks are crater-like surficial expressions of the underlying fluid and gas system (Hovland et al., 2002) that have been commonly observed on the seabed worldwide (Judd et al., 2002; Hovland et al., 2002). Estimates of global methane emission from continental shelf seeps, including pockmarks, indicate that 1.9 to 65 teragrams (Tg, 10^{12} g) of methane are being emitted annually (Trotsyuk and Avilov, 1988; Hovland and Judd, 1992; Judd et al., 2002). A fraction of this, 0.4 to 12.2 Tg, reaches the atmosphere every year and constitutes a significant portion of the global atmospheric methane emission from geological sources (3-34%, Judd et al., 2002). How much of this methane actually reaches the water column and/or atmosphere is largely determined by the efficiency of the sedimentary biology sink for methane, the "benthic filter" (Sommer et al., 2006; Boetius and Wenzhofer, 2013). Macrofauna and microbes turn methane into other dissolved ions through metabolic processes. For example, a significant fraction of methane produced in the sediments is transformed, through anaerobic oxidation of methane, to dissolved inorganic carbon (Boetius et al., 2000; Hinrichs and Boetius, 2003), which is then partially removed from solution by authigenic carbonate precipitation (von Rad et al., 1996; Luff et al., 2005; Hong et al., 2014b). Despite the surmised importance of these processes, their nature and magnitude are poorly understood (Boetius and Wenzhofer, 2013).

Along Vestnesa Ridge, northwest of Svalbard, pockmarks are commonly observed on the seafloor collocated with an underlying acoustic chimney system (Bünz et al., 2012; Petersen et al., 2010). These pockmarks contribute a significant amount of methane to the water column (Bünz et al., 2012; Smith et al., 2014). Seepage along the ridge is restricted to the eastern segment of Vestnesa Ridge (Figure 1A). The detailed 3D seismic mapping of Plaza-Faverola et al. (2015) showed the evolution of seepage for the last ~2.7 Ma. Panieri et al. (2014) and Consolaro et al. (2015) documented repeated methane emission events for the last <23 kyrs. based on the

anomalously negative carbon isotope excursions measured on benthic and planktonic foraminifera shells. Ambrose et al. (submitted) observed discrete shell beds from two sediment cores recovered in this area and suggested prolonged (*ca.* 1000 yrs.) seepage activity approximately 17 kyrs. ago. While the past and present activity of these pockmarks is well documented, no study from Vestnesa Ridge has been conducted to quantify the efficiency of sedimentary methane sinks.

To identify and quantify the various methane removal processes in the shallow sediments of Vestnesa Ridge, we measured the concentration of major ions in the pore water from five gravity cores collected in this region. We then employed numerical modeling of the pore water profiles (see *Supplementary material*) that characterized the exchange of carbon among anaerobic oxidation of methane (AOM), particulate organic matter sulfate reduction (POCSR), and authigenic carbonate precipitation (CP). We compared our model-derived rates with global datasets and estimations of methane release from the seafloor to assess the significance of our estimates. Our results reveal differences in carbon mass balance between the active and inactive pockmarks and confirm the importance of various processes/reactions in removing methane carbon from the shallow sediments along the eastern Vestnesa Ridge.

Geological Background

Vestnesa Ridge is a sedimentary drift developed under the effect of bottom currents along the west-Svalbard margin (Eiken and Hinz, 1993 and Howe et al., 2008). Despite its location on a passive margin, Vestnesa Ridge is in close proximity to active oceanic spreading ridges of Fram Strait (*e.g.,* Johnson et al., 2015) and geothermal gradients along the ridge are thus significantly higher than towards the passive margin (Crane et al., 1991). The sedimentary body consists of three main stratigraphic sequences that can be identified from seismic stratigraphy (Eiken and Hinz, 1993). The youngest sequence, YP3, is dominated by a long-slope transport and deposition from bottom currents with a major circular depocenter observed on the western Vestnesa segment (Eiken and Hinz, 1993). The middle sequence, YP2, has a depocenter parallel to the west-Svalbard margin that suggests a successive westward migration from Prins Karl Foreland (Eiken

and Hinz, 1993). The oldest sequence shows syn-rift and post-rift sedimentation on the < 19 Ma old oceanic crust (Engen et al., 2008; Johnson et al., 2015). Contourites, turbidites, and ice-rafted deposits have been commonly observed from sediments younger than mid-Weichselian on Vestnesa Ridge (Howe et al., 2008).

The Vestnesa Ridge gas hydrate system

Vestnesa Ridge hosts a deep water (> 1000 m) gas hydrate system characterized by a well-defined bottom simulating reflector (BSR) (Hustoft et al., 2009; Petersen et al., 2010). Gas hydrates have been recovered by gravity cores from some of the active pockmarks (Panieri et al., 2014; Smith et al., 2014). Seismic blanking that pierces through the gas hydrate stability zone (GHSZ) has been interpreted as gas-filled pathways. These are conduits for gas that migrates from deep hydrocarbon reservoirs toward the seafloor. Several of these gas chimneys terminate at the seabed below the observed pockmarks (Petersen et al., 2010; Bünz et al., 2012; Plaza-Faverola et al., 2015). It has been suggested that the eastern and western segments of Vestnesa Ridge are dominated by different tectonic stress fields that in turn affect the distribution and activity of seepage (Plaza-Faverola et al., 2015). We focus on three active pockmarks along the eastern Vestnesa segment (Figure 1) where gas chimneys developed along near-vertical NW-SE striking faults, interpreted as manifestation of shear deformation from the Spitsbergen Transform Fault (Plaza-Faverola et al., 2015). Abundant free gas below the GHSZ has been identified from seismic data (Hustoft et al., 2009; Figure 1C). Shallow gas accumulations as well as the presence of buried authigenic carbonate concretions and/gas hydrates at the interior of gas chimneys have been inferred by seismic anomalies in high resolution 3D seismic data (Plaza-Faverola et al., 2015). Acoustic flares detected by echosounder data from active pockmarks, extend as shallow as < 400 m below the sea surface, corresponding to the upper limit of the GHSZ for gas hydrates with thermogenic gases (Smith et al., 2014).

Analytical methods and results

We measured the concentration of major ions in the pore water from five gravity cores recovered along the eastern segment of Vestnesa Ridge during the 2008 RSS James Clark Ross (JR211)

cruise and 2013 R/V Helmer Hanssen cruise (HH13). Gravity cores were recovered from three active pockmarks with flares (JR211-26, HH13-200, and HH13-203), an inactive pockmark without a flare (HH13-197), and a background core *ca.* 200 m away from the nearest pockmark (HH13-199) (Figure 1B). Water depths of the five sites range from 1143 to 1210 meters (Table 1). Pore water sulfate and methane, which were measured from all five cores, are used to infer the depth of sulfate-methane-transition-zone (SMTZ) and estimate the strength of methane flux in the sediments. Pore water phosphate, a product of organic matter degradation, was measured from the four HH13 cores and used to infer pathways of organic matter turnover. Profiles of pore water calcium, magnesium, and strontium were determined from all five cores. These profiles reflect the rate of authigenic carbonate precipitation; an important carbon fixation pathway that turns dissolved carbon to carbonate minerals. The four HH13 cores were also examined using x-ray images to clarify the sedimentary sequence. We used GEOTEK X-ray core imaging system (MSCL-XCT 3.0) to image the archived half of the four HH13 cores. X-rays were made with an intensity of 120 keV and a resolution 20 mm. Before imaging, the archived spilt-cores were thawed in a cooling room. We dried the spilt-core surface with kimwipes and smoothed any obvious roughness to avoid interrupting the camera.

Pore water sampling and analyses for core JR211-26 were detailed in Panieri et al. (2014). For the other four sites (HH13-197, -199, -200, -203), cores were kept frozen onboard and brought back for shore-based analyses. After thawing the gravity cores in the cooling room (4°C), pore water samples were collected with rhizons (rhizon micro suction samplers: 10 cm, 0.15 μm porous polymer, Rhizosphere Research). We drilled 3.8 mm into the plastic liner at 15cm intervals and then inserted the wetted rhizons with 10 ml syringes attached. Wooden spacers were used to create a vacuum inside the syringes. The pore water collected was then filtered and diluted to proper ratios for analyses in Geological Survey of Norway (NGU) laboratories. We measured sulfate concentration by the Dionex ICS - 1100 Ion Cromatograph with a Dionex AS-DV autosampler and a Dionex IonPac AS23 column (eluent: 4.5 mM Na_2CO_3/0.8 mM $NaHCO_3$, flow: 1ml/min) and phosphate by spectrophotometry (Murphy and Riley, 1962). Prior to measuring for phosphate, concentrated HCl (10 μL) was added to 1 mL of pore water sample and left overnight to remove H_2S which will disturb the reaction forming the colour complex.

Ammonium molybdate solution (50 µL) and ascorbic acid solutions (50 µL) were well mixed with 1mL of sample in a disposable polystyrene cuvette. After the treatment, samples were stored in the dark for ten minutes to complete the reaction. Concentration of phosphate was determined photometrically with a Shimadzu UVmini-1240 UV-Vis Spectrophotometer at a wavelength of 880 nm.

The pore water chloride profiles for all sites reflect no contribution from deep fluid (Figure 2). The low chloride concentration below 2 mbsf at JR211-26 (Figure 2E) reflects the influence from gas hydrate dissociation as hydrate was recovered below the corresponding depth. Concentrations of all pore water species, except for chloride, were corrected for this influence with correction factors (corr-F) defined as:

$$\text{corr-F} = [Cl^-]_{sample}/[Cl^-]_{avg} \quad (1)$$

where $[Cl^-]_{sample}$ is the measured chloride concentration with the influence of hydrate dissociation at each depth and $[Cl^-]_{avg}$ is the average chloride concentration for samples above 2 mbsf at this site (~558.6 mM), the samples that are free from the influence of gas hydrate dissociation.

For the three active pockmark sites (HH13-200, HH13-203, and JR211-26), the concentrations of all pore water species are constant and close to bottom seawater composition for the first 50-70 cm in the sediments and then decrease or increase rapidly (the "kinked" profiles hereafter) (Figures 2C, 2D, and 2E). The SMTZ is shallow at these three sites (0.8-1.2 mbsf, Table 1), compared to the other two sites (> 3 mbsf for HH13-197 and HH13-199, Figures 2A and 2B), suggesting a stronger methane flux at the active pockmarks. The kinked pore water profiles are clear signs of a non-steady-state condition that is due to recent and dynamic changes in either sediments or pore water (Zabel and Schulz, 2001; Hensen et al., 2003; Haeckel et al., 2007; Holstein and Wirtz, 2010; Hong et al., 2014a). Higher phosphate concentration for the non-active pockmark sites compared to active pockmarks is interpreted as faster organic matter degradation

rates and different sulfate reduction pathways. Rapid reduction in the concentrations of calcium, magnesium, and strontium from the three active pockmark sites indicates active authigenic carbonate precipitation that is promoted by the fast production of bicarbonate from AOM (Luff and Wallmann, 2003; Snyder et al., 2007; Wallmann et al., 2006a; Hong et al., 2014b). No authigenic carbonate, however, was observed.

The x-ray images and visual observation of the cores revealed mostly homogeneous dark or grey clay with occasional isolated clasts (Figure 3). Porosity was only measured at JR211-26. It is generally low and quite constant throughout the core (0.78 to 0.62; mean= 0.68, SD=0.03, n=19).

Model Setup

We developed two sets of models to quantify the biogeochemistry and hydrology in the sediments. In one set of models, we use CrunchFlow, a code designed to simulate solute diffusion and biogeochemical reactions (Steefel, 2009), to investigate and quantify the biogeochemical reactions under steady-state conditions. We included no advection component in this steady-state model as, based on the age of sediment (14 kyr, Consolaro et al., 2014) and the calculation of Péclet number (Pe=10^{-2} to 10^{-1}), advection is of very little importance compared to diffusion. We noticed non-steady-state behavior in the shallow part (<50-70 cm below seafloor) of the pore water system (see the *Results* section for more details). As a result, we further investigated this non-steady state behavior by coupling CrunchFlow with a MATLAB routine that we developed to simulate fluid advection. From the results of this modeling, we show that such non-steady-state was a short-term process and therefore does not undermine our assumption of steady state in the other model. We summarize the numerical framework of both models, the parameters used, and the boundary and initial conditions in the *Supplementary material*.

We consider three primary reactions in our model: particulate organic matter sulfate reduction (POCSR), anaerobic oxidation of methane (AOM), and authigenic carbonate precipitation (CP). Organic matter is consumed by sulfate (*i.e.*, POCSR) upon burial through microbial activities following the stoichiometry:

$$(CH_2O)(NH_3)_{\frac{19}{112}}(H_3PO_4)_{\frac{1}{112}} + 0.5SO_4^{2-} \rightarrow 0.5HS^- + 0.6516HCO_3^{2-} + 0.1695NH_4^+ + 0.008929HPO_4^{2-} + 0.3484CO_2 + 0.3484H_2O \quad (2)$$

We used 5.9 and 112 for C/N and C/P, respectively; ratios obtained from sediment trap data at a location very close to our study sites with similar water depth (Tamelander et al., 2012). Accumulation of dissolved inorganic carbon (DIC) and methane inhibit organic matter degradation (Wallmann et al., 2006a). Such effects are considered in our model by implementing two inhibit terms (see *Supplementary material*).

A significant fraction of the pore water sulfate is consumed at the SMTZ through anaerobic oxidation of methane (AOM):

$$CH_{4(aq)} + SO_4^{2-} \rightarrow HCO_3^- + HS^- + H_2O \quad (3)$$

We assumed that all methane fueling AOM originates below our model regime, which accounts for any methane source that is located deeper than the sample depth. Methanogenesis from organic matter is excluded in our model domain, a choice justified by the small increase of phosphate concentration below the sulfate reduction zone (Figure 2).

Rapid AOM fueled by strong methane supply stimulates the precipitation of authigenic carbonate, which is obvious from the pore water calcium, magnesium, and strontium profiles (Figure 2). We included both Ca-calcite and Mg-calcite in the model to account for such observations:

226 $(Ca, Mg)\ CO_{3(s)} + H^+ \rightarrow (Mg^{2+}, Ca^{2+}) + HCO_3^-$ (4)

227

228 To correctly account for the change of pH and alkalinity in the dissolved phase, we also included
229 different speciation of dissolved carbonate, ammonium, and phosphate. Dissolution of CO_2 and
230 CH_4 gases were also included although the model was set to be always water saturated (*i.e.,* no
231 gas phase transport). The full list of these secondary reactions and their respective equilibrium
232 constants are included in Hong et al. (2014).

233

234 **Results and discussion**

235 *Quantifying the non-steady state condition of the pore water system*

236 Several processes have been proposed to explain kinked pore water profiles (Figure 2C to 2E): (1)
237 The sediment section with constant and near-seawater concentration may have been recently
238 deposited by mass movements of sediments, slumps, and/or slope failures (Zabel and Schulz,
239 2001; Hong et al., 2014a). Under this scenario, related sedimentary features such as complex
240 folding, crumpling, deformation structures, or imbricated mud clasts (Van Daele et al., 2014;
241 Baeten et al., 2014) should be observed in the sediments; (2) Exchange of bottom seawater by
242 infaunal animals or bioturbation. Animal burrows or traces from animal movements should be
243 evident in the sediments if bioturbation is important (O'Brien, 1987; Britt et al., 1992; Löwemark
244 and Werner, 2001; Rebesco et al., 2013); (3) Enhanced exchange between bottom seawater and
245 pore fluid due to irrigation by ascending methane bubbles from sub-seafloor (Haeckel et al., 2007;
246 Chuang et al., 2013); (4) Downward flow of bottom seawater into the shallow sediments
247 ("aqueous pump" hereafter) as proposed by Tryon et al. (1999). The aqueous pump mechanism
248 refers to the invasion of bottom seawater due to vigorous seeping of fluid in adjacent sediments.
249 Expelling of fluid from the adjacent sediments causes imbalance in hydraulic pressure, especially
250 in shallow sediments where sediments are not yet consolidated, and results in bottom seawater
251 invasion (Tryon et al., 1999; Figure 4A).

252

From the x-radiographs and our visual inspection (Figure 3), we observed no sedimentary features that can support the existence of geological events, bioturbation, and bubble irrigation. As concluded by Haeckel et al. (2007), to stimulate an eddy diffusion that is strong enough to result in the kinked porewater profile, a tube radius of 1 cm is required, which we did not observe during our visual inspection. Collectively, the aqueous pump mechanism is the most likely processes that can explain our observations from porewater profiles. The coincidence that the kinks are only obvious at the sites with shallow SMTZ (Figure 2C to 2E) suggests that these sites are closer to the center of active seepage, where methane flux is strongest, and therefore consistent with the postulate of an aqueous pumping mechanism.

From our simulation of fluid flow, we estimate the rate of fluid flow as well as the duration of aqueous pumping. We are only able to constrain the minimum value of fluid velocity and the largest time span for such downward fluid flow since diffusion tends to smooth the kinked pore water profiles if the advection term is too small. Our model estimates that, for the three pockmark sites, the aqueous pump has been operating for at most ~1 to 1.8 years (Figure 4C to 4E) and the minimum fluid flux required ranges from 0.6 to 0.3 m/yr. for the three sites. The resulting velocities are similar to what was measured in Hydrate Ridge (Tryon et al., 2002) and Gulf of Mexico (Solomon et al., 2008). We do not expect any distortion in the sediment structure under such low flow rate since the fluid velocity has to be a few orders of magnitude higher than our estimates to cause failure in sedimentary structure (Mörz et al., 2007).

Assuming the aqueous pump is associated with pockmark activity, the kinked pore water profiles reflect current activity that is no more than 1.8 years old. Few studies have monitored seeping activity long term (>1 year). Solomon et al. (2008) monitored a seep site in the Gulf of Mexico with flow meters for more than 400 days. Tryon et al. (2012) deployed benthic chambers around seafloor venting in the Sea of Marmara for 13 months. Both records show pulses of strong fluid flow that lasted for several months, which are in agreement with the duration we estimated from our pore water profiles. As the aqueous pump process is a rather short-term process, it does not undermine our steady-state assumption for the carbon mass balance model.

282

283 *Mass balance of carbon under steady state assumption*

284 Based on the assumed biogeochemical reaction network, our model estimates the steady-state
285 rates of AOM, POCSR, and CP. The rates of both POCSR and CP are constrained by the pore
286 water profiles of phosphate, calcium, and magnesium. AOM rates thus equal the sulfate
287 consumption not associated with POCSR. We integrated over the depth range for which the rate
288 of each reaction is significantly higher than the background and express them as depth-integrated
289 rates (Table 1). These rates were expressed as the amount of dissolved inorganic carbon (DIC, the
290 sum of bicarbonate, carbonate, and dissolved CO_2) produced or consumed for comparison
291 purposes. The rate of total SR is the overall sulfate reduction from AOM and POCSR. Methane
292 flux from the bottom of our model regime can be inferred from the AOM rate as we included no
293 other methane source in our model.

294

295 Our model results indicate a difference in carbon mass balance between the active pockmark sites
296 and the non-active sites. AOM rates are 1 to 3 orders of magnitudes higher in the active sites than
297 the non-active sites. There are only trace amounts of dissolved methane in the sulfate reduction
298 zone (< 50 μM, Figure 2) from the active sites suggesting the rapid consumption of methane at
299 the SMTZ. The pore water data, therefore, show that AOM in the sediment can effectively
300 remove methane and prevent it from reaching the overlying seawater. The efficiency of AOM at
301 removing dissolved methane from sediment is especially evident at JR211-26 where gas hydrate
302 was recovered below 2 mbsf. To sustain such shallow gas hydrate reservoir, a kinetically-
303 controlled gas-water-hydrate system is required (Torres et al., 2004; Liu and Flemings, 2006; Cao
304 et al., 2013) which also implies potentially higher dissolved methane concentration compared to a
305 system without free gas (Cao et al., 2013). It should be emphasized that even with such a shallow
306 gas hydrate reservoir and potentially coexisting higher dissolved methane content, both AOM and
307 aqueous pumping seal virtually all methane in the sediments at this site.

308

309 Such a result seems to contradict the general observations of acoustic flares in the water column
310 along Vestnesa Ridge (*e.g.,* Bünz et al., 2012 and Smith et al., 2014). Seeping of gas bubbles in

an area of a few m^2 or km^2 as revealed by echosounder surveys may be a common phenomenon in the area, but the spatial distribution of such degassing is in fact very heterogeneous. Seafloor observations of other cold seeps worldwide show that escaping of gas bubbles concentrate in an area of a few tens of cm^2 (*e.g.,* MacDonald et al., 1996; Haeckel et al., 2004; Nikolovska et al., 2008). The area surrounding sites of escaping gas shows no signs of degassing even though they may be close to a seeping center. It is likely that our cores with shallow SMTZ (*i.e.,* HH13-200, HH13-203, and JR211-26) were collected close to seeping centers but not directly over a site of degassing. Our pore water profiles and modeling show that AOM can effectively remove dissolved methane from the sediment when there is strong methane flux but not apparent degassing from the sea floor.

The strong methane fluxes and the resulting AOM stimulate 3 to 10 times more carbonate precipitation at the active sites than the other two sites with weaker methane fluxes (Table 1). The rapid production of bicarbonate by AOM is responsible for most of the CP rate differences between active and non-active sites. For the three active sites, methane carbon is transformed to DIC at a rate of 29.77 to 41.87 μmol/cm^2/yr. A significant fraction of this DIC production, 8.25 to 10.08 μmol/cm^2/yr or 25 to 29% of the total AOM rate precipitates as authigenic carbonate by reacting with pore water calcium and magnesium. Such authigenic carbonate precipitation therefore serves as a very important sink for dissolved carbon in the sediments. The CP rates we estimated from the active pockmarks sites are similar to the rates estimated from Hydrate Ridge (115.5 μmol DIC/cm^2/yr; Luff and Wallmann, 2003) and an order of magnitude higher than the rates in Ulleung Basin (0.4-2.6 μmol DIC/cm^2/yr; Hong et al., 2014b), Sea of Okhotsk (2.96 to -0.054 μmol DIC/cm^2/yr; Wallmann et al., 2006a), and Umitaka Spur (1.93 to 0.97 μmol DIC/cm^2/yr; Snyder et al., 2007; assuming the calcium and magnesium fluxes are equivalent to calcification rates). Our estimations also fall at the high end of the global range (Sun and Turchyn 2014). Such high CP rates should result in the accumulation authigenic carbonate in the sediments of active pockmarks along eastern Vestnesa Ridge. Panieri et al. (2014) documented calcite overgrowth on the outside of foraminifera shells. This overgrowth has a depleted carbon isotopic signature compared to the biogenic tests and suggests a link with methane emission (Panieri et al., 2014). Ambrose et al. (submitted) also observed the presence of carbonate

341 concretions in the sediments from core HH 13-203. Although not from Vestnesa Ridge, Chow et
342 al. (2000) reported detailed geochemical studies on the authigenic carbonate found from ODP
343 Site 909, a site drilled a few kilometers south of Vestnesa Ridge. From the elemental composition
344 of these Fe-Mn carbonates with enriched calcium and magnesium, Chow et al. (2000) suggested
345 these carbonates might precipitate in the suboxic zone of sediments, from the Fe-reduction to the
346 early methanogenesis zone.

347

348 The proportion of sulfate consumed by POCSR at the two non-active sites covers a wide range,
349 from 13.1 to 97%, whereas almost all sulfate is consumed by AOM at the active sites (Table 1).
350 At sites HH13-197 and -199, active POCSR lowers pH by adding CO_2 to the system (Eq. (2)) and
351 therefore dissolves carbonate minerals. Authigenic carbonate precipitation was suppressed for the
352 first meter at these two sites due to active POCSR over this depth (Figure 2A and 2B). The
353 modeling done by Luff et al. (2001) and Jourabchi et al. (2005) also shows decreasing pH when
354 organic matter degradation dominates.

355

356 *Pore water phosphate as an indication of organic matter turnover*

357 Contrasting levels of phosphate among sites (Figure 2) suggest different organic matter
358 degradation rates and resulting sulfate reduction pathways. For sites with abundant methane
359 supply (*i.e.,* shallow SMTZ), AOM is stimulated by the increasing methane supply from below.
360 POCSR is less active under this condition as most sulfate reacts with methane through AOM. We
361 account for this effect by using a small kinetic constant for POCSR in our steady-state simulation
362 (Table S1 in *Supplementary material*). On the other hand, when the pockmark activity wanes,
363 more sulfate is available for POCSR which results in the higher phosphate level observed from
364 the inactive sites. We therefore need to use a larger kinetic constant to describe this scenario in
365 our model.

366

367 If we assume the same organic matter composition (*i.e.,* similar reactiveness and C/P ratio) for
368 all the study sites, the factor controlling the level of pore water phosphate is the time duration of
369 organic matter degradation; *i.e.,* more phosphate is released when organic matter is degraded for

a longer time. We modified our steady-state model to estimate how long organic matter has been degraded at the four HH13 sites. We used the kinetic constant from site HH13-199, a site that has minimum influence from AOM as we did not penetrate the sulfate reduction zone at this site with our 5-meter gravity core. AOM was inhibited in this model run and we used a no flux lower boundary condition assuming no input of phosphate below the model regime. We adopted these crude assumptions to provide a first-order estimation of the length of time that organic matter has been actively consumed by sulfate (*i.e.*, POCSR). The variation in C/P molar ratios (112±12) reported by Tamelander et al. (2015) results in a 25-year uncertainty in our age estimation. Our model suggests that it takes ~350 to 550 years for POCSR to produce the amount of phosphate observed at sites HH13-197 and HH13-199 (Figure 5) and less than 50-100 years for sites HH13-200 and HH13-203 (Figure 5). The short POCSR effective time for the two active pockmark sites implies that most sulfate has *not* been consumed by POCSR. This model result therefore delivers an important message: most pore water sulfate at the two active pockmark sites was consumed by the methane-fueled AOM for the past approximately two to four centuries. Methane flux has to be persistently strong during this time period. The 50-100 years gap at the two active sites when methane supply waned and sulfate was available for POCSR is probably the sum of many short-term gaps that occurred throughout the entire active periods. It is very unlikely to have interruptions between methane supply episodes for more than a few decades as organoclastic sulfate reduction will be in effect as soon as sulfate is available for reaction and therefore produces phosphate.

Together with the 1 to 1.8 years long aqueous pumping we estimated by modeling the kinked porewater profiles, we interpret both frequencies, year-long and centurial-scale, as seeping activities modulated by processes of different time scales. The aqueous pumping represents the short-term “breaths” of the pockmarks while the supply of methane, which may be related to the stress field at depth (Plaza-Faverola et al., 2015), can be several centuries long, as we estimated from the phosphate profiles.

Ambrose et al. (submitted) observed a high concentration of bivalve shells and fragments spanning 30 cm (2.36-2.68 mbsf) in core HH13-203, the same core we investigated. The bivalves

in this "clam bed" were dominated by two genera of the Vesiscoymidae which are dependent on sulfide-reducing endosymbioitc bacteria for nutrition (Krylova and Shaling, 2010). These bivalves, therefore, can only survive under conditions of persistent methane flux and the age of an individual bivalve is, therefore, an estimate of the minimum length of time of strong methane emission. By counting the number of rings in the hinge of one large individual (*Phreagena* s.l.), and assuming the lines to be annual the clam was estimated to be 20-25 years old (Ambrose unpublished data). Deepsea bivalves that have been investigated are known to deposit daily growth lines apparently with a tidal rhythm (Schöne and Giere, 2005; Nedoncelle et al., 2013), but none have been investigated for annual lines so the age estimate is speculative. The clam bed in the core persisted for approximately 1000 years from 17,707 to 16,680 years ago. The 1000-year duration of seeping constrained by the presence of bivalves in the core is longer than, but similar to, the length of time we estimated based on the phosphate profiles (200-400 years). This suggests that the site was subject to several seeping events in the past with events ranging in duration from a few centuries to a thousand years.

Fate of methane in Vestnesa Ridge sediments

The significance of AOM as an important dissolved methane sink has been widely appreciated for decades (Hinrichs and Boetius, 2003; Knittel and Boetius, 2009; Regnier et al., 2011; Boetius and Wenzhofer, 2013). Quantification of AOM rates by experiment or modeling techniques, however, has received far less attention (Knittel and Boetius, 2009; Regnier et al., 2011; Boetius and Wenzhofer, 2013). Our effort to quantify AOM along Vestnesa Ridge adds another estimate in the Arctic, where such estimates are scarce (Regnier et al., 2011). Comparing our estimates with the global model-derived AOM rates compiled by Regnier et al. (2011), our results fall in the center of the data cluster (Figure 6). Extrapolating from our four estimates (excluding HH13-199) to the point where the depth of SMTZ is only 2 cm, the shallowest SMTZ ever reported from the Black Sea and Hydrate Ridge (Treude et al., 2003; Wallmann et al., 2006b), we can approximate the maximum AOM rate (1600 μmol/cm^2/yr, *b* in Table 2) at the near-center of pockmarks from Vestnesa Ridge (Figure 7). This rate is likely to be even higher if the SMTZ is shallower than 2 cm (*b* in Table 2). The maximum AOM rate we estimate is in agreement with the highest model-derived rate (Regnier et al. 2011) and the highest *in-situ* rate ever reported in

Hydrate Ridge (Treude et al., 2003; Boetius and Wenzhofer, 2013) (*c* and *d* in Table 2). The next question will be how does such a high AOM consumption rate compare with the output of methane from seafloor to water column.

Wide-spread acoustic flares have been well-documented along Vestnesa Ridge (*e.g.,* Bünz et al., 2012 and Smith et al., 2014) although no output of methane has yet, to the best of our knowledge, been quantified in this region. The estimations of methane output at Prins Karl Foreland (PKF), the shallow-water seep sites west of Svalbard, suggest an output of more than 144 tons/year of methane (*e* in Table 2). It is likely that such methane output from PKF is higher than the output from the pockmarks along Vestnesa Ridge since PKF is considered to be more active due to its location (Westbrook et al., 2009; Berndt et al., 2014). The precise estimation of methane output in the water column of Vestnesa Ridge awaits future studies. By integrating the AOM rate we estimated over the area of the pockmark (assuming 10 meters or 100 meters radius), AOM consumes only 0.05 to 0.21 tons of methane annually, a small fraction of the output estimated from acoustic flares (*a* in Table 2).

The different estimation in AOM rates and escaping output of methane may be partly due to the uncertainties and limitations associated with both methods of measurements. Our extrapolation of the maximum methane consumption by AOM depends to a large extend on the depth of the SMTZ. The consumption increases ~100-fold when the depth of the SMTZ varies by a factor of 10 (*b* in Table 2). Such an increase in consumption is, however, counterbalanced by the smaller area covered by such focused consumption. The annual rate of methane consumption is likely to be the order of 100 kg (0.1 tons) per year which would be the highest rate recorded globally (Regnier et al. 2011; Boetius and Wenzhofer 2013).

There are uncertainties in the hydroacoustic method for quantifying gas bubble flow rate (Veloso et al. 2015). By comparing the models from several investigators, Velosco et al. (2015) concluded that the relative error can be as much as 60%. Furthermore, in order to convert flow rate to methane output, one must know the concentration of methane in bubbles, a parameter that

459 is assumed to be 100% methane in PKF based on the measurements done by Sahling et al. (2014)
460 at one seep. This concentration may be temporally and spatially variable. Boetius and Wenzhofer
461 (2013) compiled *in-situ* benthic chamber measurements that determine the flux of methane
462 leaving surficial sediments from seeps worldwide. The flux ranges from several hundred to
463 44,749 μmol/cm^2/yr (*f* in Table 2). In order to arrive at an estimate similar to the values reported
464 at PKF, we have to assume the highest flux seeping from an area with radius of 100 m (*f* in Table
465 2), which is an unreasonable assumption. It is beyond the scope of our paper to resolve the
466 different estimations made by different methods. We note, however, the importance of such an
467 exercise to comprehensively understand the fate of methane in sediments. Despite all the
468 uncertainties, we may still conclude that AOM consumes a rather small fraction of methane in the
469 Vestnesa Ridge surficial sediments compared to what escapes from the seafloor, although the
470 exact fraction is still unclear.

471

472 **Summary**

473 Vestnesa Ridge has been confirmed by both the mapping of fluid pathways in the sediments and
474 acoustic flares in the water column to be an area of high levels of methane seepage from the
475 seafloor (Petersen et al., 2010; Bünz et al., 2012; Smith et al., 2014). The potential discharges of
476 methane from geosphere to hydrosphere are nevertheless speculative (Bünz et al., 2012; Smith et
477 al., 2014). The biological and chemical reactions at, or near, the sediment surface represent the
478 last line of defense preventing dissolved methane from escaping the sediments. We model the
479 efficiency of these processes in filtering methane at Vestnesa Ridge and show that dissolved
480 methane in the shallow sediments (<5 mbsf) is consumed or diluted through hydrological,
481 microbial, and geochemical processes/reactions (Figure 7).

482 - We attribute the kinked pore water profiles from the three active pockmark sites as the
483 consequence of seepage-related pressure imbalance and the resulting bottom sea water
484 intrusion. Such intrusion dilutes the concentration of methane in the first 50-70 cm of
485 sediments and effectively prevents methane from leaking to the overlying bottom water.
486 By fitting observed sulfate profiles, our model suggests there has been 1 to 1.8 years of
487 continuous downward flow of bottom seawater at a velocity of 0.3 to 0.6 m/yr. This

process provides a short-term negative feedback to the seepage activity of the active pockmarks.

- The results of our steady-state model confirm efficient dissolved methane removal through AOM at the active sites. For the three active pockmarks, 29.3 to 40.9 μmol/cm^2/yr of methane is converted to DIC, a regulation of dissolved methane concentration in the sediments for centurial time scale. From the modeling of phosphate profiles, we show that AOM has been persistently active for at last 2-4 centuries at the three active pockmarks. It is worth noting that, due to the high efficiency of AOM, virtually no dissolved methane escapes from the sediments even at the site where gas hydrate is present below 2 mbsf. AOM may seem to be inefficient because of the documented methane that escapes into the water column. Comparing the efficiency of AOM at removing methane to the amount of methane in the water column is, however, fraught with uncertainty due to assumptions and limitations inherit in the different methods.
- The ultimate sink for methane carbon is the precipitation of authigenic carbonates, the reaction that sequestrates methane over geological time scale. We estimated that 25% to 29% of the methane carbon is ultimately fixed as authigenic carbonates at the active pockmarks.

Acknowledgement

The authors would like to thank the captains, crew members, and scientific parties of both 2008 RSS James Clark Ross cruise and 2013 R/V Helmer Hanssen cruise. This work was supported by the Research Council of Norway through its Centres of Excellence funding scheme, project number 223259. W.G.A. Jr. is now an employee of the US NSF, however any opinion, finding, and conclusions or recommendations expressed in this material are those of W.G.A. Jr. and his coauthors, and do not necessarily reflect the views of the US NSF. We thank Dr. JoLynn Carroll for comments on the earlier version of this manuscript and Joanne Muratori for editorial assistance.

References

Ambrose , W. G. Jr., Panieri, G., Schneider, A., Plaza-Faverola, A., Carroll, M., Åstrøm, K., Locke V, W., and Carroll, J., 2015, Vesicomyid bivalve community indicates prolonged past emission in the Arctic Ocean: (in review).

Baeten, N. J., Laberg, J. S., Vanneste, M., Forsberg, C. F., Kvalstad, T. J., Forwick, M., Vorren, T. O., and Haflidason, H., 2014, Origin of shallow submarine mass movements and their glide planes—Sedimentological and geotechnical analyses from the continental slope off northern Norway: Journal of Geophysical Research: Earth Surface, v. 119, no. 11, p. 2335-2360.

Berndt, C., Feseker, T., Treude, T., Krastel, S., Liebetrau, V., Niemann, H., Bertics, V. J., Dumke, I., Dünnbier, K., Ferré, B., Graves, C., Gross, F., Hissmann, K., Hühnerbach, V., Krause, S., Lieser, K., Schauer, J., and Steinle, L., 2014, Temporal Constraints on Hydrate-Controlled Methane Seepage off Svalbard: Science, v. 343, no. 6168, p. 284-287.

Boetius, A., Ravenschlag, K., Schubert, C. J., Rickert, D., Widdel, F., Gieseke, A., Amann, R., Jorgensen, B. B., Witte, U., and Pfannkuche, O., 2000, A marine microbial consortium apparently mediating anaerobic oxidation of methane: Nature, v. 407, no. 6804, p. 623-626.

Boetius, A., and Wenzhofer, F., 2013, Seafloor oxygen consumption fuelled by methane from cold seeps: Nature Geoscience, v. 6, no. 9, p. 725-734.

Britt, S. L., Bottjer, D. J., Fischer, A. G., Flocks, J. G., and Gorsline, D. S., 1992, X-radiography of horizontal core slabs - a method for greater retrieval of sediment core data: Journal of Sedimentary Petrology, v. 62, no. 4, p. 718-721.

Bünz, S., Polyanov, S., Vadakkepuliyambatta, S., Consolaro, C., and Mienert, J., 2012, Active gas venting through hydrate-bearing sediments on the Vestnesa Ridge, offshore W-Svalbard: Marine Geology, v. 332–334, no. 0, p. 189-197.

Cao, Y., Chen, D., and Cathles, L. M., 2013, A kinetic model for the methane hydrate precipitated from venting gas at cold seep sites at Hydrate Ridge, Cascadia margin, Oregon: Journal of Geophysical Research: Solid Earth, v. 118, no. 9, p. 4669-4681.

Chow, N., Morad, S., and Al-Aasm, I. S., 2000, Origin of authigenic Mn-Fe carbonates and pore-water evolution in marine sediments: evidence from Cenozoic strata of the Arctic Ocean and Norwegian-Greenland Sea (ODP Leg 151): Journal of Sedimentary Research, v. 70, no. 3.

Chuang, P. C., Dale, A. W., Wallmann, K., Haeckel, M., Yang, T. F., Chen, N. C., Chen, H. C., Chen, H. W., Lin, S., Sun, C. H., You, C. F., Horng, C. S., Wang, Y. S., and Chung, S. H., 2013, Relating sulfate and methane dynamics to geology: Accretionary prism offshore SW Taiwan: Geochemistry Geophysics Geosystems, v. 14, no. 7, p. 2523-2545.

Consolaro, C., Rasmussen, T. L., Panieri, G., Mienert, J., Bünz, S., and Sztybor, K., 2014, Carbon isotope ($\delta^{13}C$) excursions suggest times of major methane release during the last 14 ka in Fram Strait, the deep-water gateway to the Arctic: Climate of the Past, v. 10, no. 5, p. 4191-4227.

Crane, K., Sundvor, E., Buck, R., and Martinez, F., 1991, Rifting in the northern Norwegian-Greenland Sea: Thermal tests of asymmetric spreading: Journal of Geophysical Research: Solid Earth (1978–2012), v. 96, no. B9, p. 14529-14550.

Eiken, O., and Hinz, K., 1993, Contourites in the Fram Strait: Sedimentary Geology, v. 82, no. 1, p. 15-32.

Engen, Ø., Faleide, J. I., and Dyreng, T. K., 2008, Opening of the Fram Strait gateway: a review

of plate tectonic constraints: Tectonophysics, v. 450, no. 1, p. 51-69.
Greinert, J., Veloso, M., De Batist, M. A., and Mienert, J., Hydroacoustic quantification of free-gas venting offshore Svalbard, Arctic: Changes in space and time, *in* Proceedings AGU Fall Meeting Abstracts2013, Volume 1, p. 07.
Haeckel, M., Boudreau, B. P., and Wallmann, K., 2007, Bubble-induced porewater mixing: A 3-D model for deep porewater irrigation: Geochimica Et Cosmochimica Acta, v. 71, no. 21, p. 5135-5154.
Haeckel, M., Suess, E., Wallmann, K., and Rickert, D., 2004, Rising methane gas bubbles form massive hydrate layers at the seafloor: Geochimica et Cosmochimica Acta, v. 68, no. 21, p. 4335-4345.
Hensen, C., Zabel, M., Pfeifer, K., Schwenk, T., Kasten, S., Riedinger, N., Schulz, H. D., and Boettius, A., 2003, Control of sulfate pore-water profiles by sedimentary events and the significance of anaerobic oxidation of methane for the burial of sulfur in marine sediments: Geochimica et Cosmochimica Acta, v. 67, no. 14, p. 2631-2647.
Hinrichs, K. U., and Boetius, A., 2003, The anaerobic oxidation of methane: new insights in microbial ecology and biogeochemistry, *in* Wefer, G., Billett, D., Hebbeln, D., Jorgensen, B., Schluter, M., and van Weering, T., eds., Ocean Margin Systems: Verlag Berlin Heidelberg Germany, Springer, p. 457-477.
Holstein, J. M., and Wirtz, K. W., 2010, Organic matter accumulation and degradation in subsurface coastal sediments: a model-based comparison of rapid sedimentation and aquifer transport: Biogeosciences, v. 7, no. 11, p. 3741-3753.
Hong, W.-L., Solomon, E. A., and Torres, M. E., 2014a, A kinetic-model approach to quantify the effect of mass transport deposits on pore water profiles in the Krishna–Godavari Basin, Bay of Bengal: Marine and Petroleum Geology, v. 58, p. 223-232.
Hong, W.-L., Torres, M. E., Kim, J.-H., Choi, J., and Bahk, J.-J., 2014b, Towards quantifying the reaction network around the sulfate–methane-transition-zone in the Ulleung Basin, East Sea, with a kinetic modeling approach: Geochimica et Cosmochimica Acta, v. 140, no. 1, p. 127-141.
Hovland, M., Gardner, J. V., and Judd, A. G., 2002, The significance of pockmarks to understanding fluid flow processes and geohazards: Geofluids, v. 2, no. 2, p. 127-136.
Hovland, M., and Judd, A. G., 1992, The global production of methane from shallow submarine sources: Continental Shelf Research, v. 12, no. 10, p. 1231-1238.
Howe, J. A., Shimmield, T. M., Harland, R., and Eyles, N., 2008, Late Quaternary contourites and glaciomarine sedimentation in the Fram Strait: Sedimentology, v. 55, no. 1, p. 179-200.
Hustoft, S., Bünz, S., Mienert, J., and Chand, S., 2009, Gas hydrate reservoir and active methane-venting province in sediments on< 20 Ma young oceanic crust in the Fram Strait, offshore NW-Svalbard: Earth and Planetary Science Letters, v. 284, no. 1, p. 12-24.
Johnson, J. E., Mienert, J., Plaza-Faverola, A., Vadakkepuliyambatta, S., Knies, J., Bünz, S., Andreassen, K., and Ferré, B., 2015, Abiotic methane from ultraslow-spreading ridges can charge Arctic gas hydrates: Geology, v. 43, no. 5, p. 371-374.
Jourabchi, P., Van Cappellen, P., and Regnier, P., 2005, Quantitative interpretation of pH distributions in aquatic sediments: a reaction-transport modeling approach: American Journal of Science, v. 305, no. 9, p. 919-956.
Judd, A. G., Hovland, M., Dimitrov, L. I., Garcia-Gil, S., and Jukes, V., 2002, The geological methane budget at Continental Margins and its influence on climate change: Geofluids, v. 2, no. 2, p. 109-126.

Knittel, K., and Boetius, A., 2009, Anaerobic oxidation of methane: progress with an unknown process: Annual review of microbiology, v. 63, p. 311-334.
Krylova, E. M., and Sahling, H., 2010, Vesicomyidae (Bivalvia): current taxonomy and distribution: PLoS One, v. 5, no. 4, p. e9957.
Liu, X. L., and Flemings, P. B., 2006, Passing gas through the hydrate stability zone at southern Hydrate Ridge, offshore Oregon: Earth And Planetary Science Letters, v. 241, no. 1-2, p. 211-226.
Löwemark, L., and Werner, F., 2001, Dating errors in high-resolution stratigraphy: a detailed X-ray radiograph and AMS-14 C study of Zoophycos burrows: Marine Geology, v. 177, no. 3, p. 191-198.
Luff, R., Greinert, J., Wallmann, K., Klaucke, I., and Suess, E., 2005, Simulation of long-term feedbacks from authigenic carbonate crust formation at cold vent sites: Chemical Geology, v. 216, no. 1-2, p. 157-174.
Luff, R., Haeckel, M., and Wallmann, K., 2001, Robust and fast FORTRAN and MATLAB (R) libraries to calculate pH distributions in marine systems: Computers & Geosciences, v. 27, no. 2, p. 157-169.
Luff, R., and Wallmann, K., 2003, Fluid flow, methane fluxes, carbonate precipitation and biogeochemical turnover in gas hydrate-bearing sediments at Hydrate Ridge, Cascadia Margin: Numerical modeling and mass balances: Geochimica Et Cosmochimica Acta, v. 67, no. 18, p. 3403-3421.
MacDonald, I., Guinasso, N., Sassen, R., Brooks, J., Lee, L., and Scott, K., 1994, Gas hydrate that breaches the sea floor on the continental slope of the Gulf of Mexico: Geology, v. 22, no. 8, p. 699-702.
Murphy, J., and Riley, J. P., 1962, A modified single solution method for the determination of phosphate in natural waters: Analytica chimica acta, v. 27, p. 31-36.
Mörz, T., Karlik, E. A., Kreiter, S., and Kopf, A., 2007, An experimental setup for fluid venting in unconsolidated sediments: New insights to fluid mechanics and structures: Sedimentary Geology, v. 196, no. 1-4, p. 251-267.
Nedoncelle, K., Lartaud, F., De Rafelis, M., Boulila, S., and Le Bris, N., 2013, A new method for high-resolution bivalve growth rate studies in hydrothermal environments: Marine biology, v. 160, no. 6, p. 1427-1439.
Nikolovska, A., Sahling, H., and Bohrmann, G., 2008, Hydroacoustic methodology for detection, localization, and quantification of gas bubbles rising from the seafloor at gas seeps from the eastern Black Sea: Geochemistry, Geophysics, Geosystems, v. 9, no. 10.
O'Brien, N. R., 1987, The effects of bioturbation on the fabric of shale: Journal of Sedimentary Research, v. 57, no. 3.
Panieri, G., James, R. H., Camerlenghi, A., Westbrook, G. K., Consolaro, C., Cacho, I., Cesari, V., and Cervera, C. S., 2014, Record of methane emissions from the West Svalbard continental margin during the last 23.500 yrs revealed by $\delta^{13}C$ of benthic foraminifera: Global and Planetary Change, v. 122, p. 151-160.
Petersen, C. J., Bünz, S., Hustoft, S., Mienert, J., and Klaeschen, D., 2010, High-resolution P-Cable 3D seismic imaging of gas chimney structures in gas hydrated sediments of an Arctic sediment drift: Marine and Petroleum Geology, v. 27, no. 9, p. 1981-1994.
Plaza-Faverola, A., Bünz, S., Johnson, J. E., Chand, S., Knies, J., Mienert, J., and Franek, P., 2015, Role of tectonic stress in seepage evolution along the gas hydrate-charged Vestnesa Ridge, Fram Strait: Geophysical Research Letters, v. 42, no. 3, p. 2014GL062474.
Rebesco, M., Wåhlin, A., Laberg, J. S., Schauer, U., Beszczynska-Möller, A., Lucchi, R. G.,

Noormets, R., Accettella, D., Zarayskaya, Y., and Diviacco, P., 2013, Quaternary contourite drifts of the Western Spitsbergen margin: Deep Sea Research Part I: Oceanographic Research Papers, v. 79, no. 0, p. 156-168.

Regnier, P., Dale, A. W., Arndt, S., LaRowe, D. E., Mogollon, J., and Van Cappellen, P., 2011, Quantitative analysis of anaerobic oxidation of methane (AOM) in marine sediments: A modeling perspective: Earth-Science Reviews, v. 106, no. 1-2, p. 105-130.

Sahling, H., Römer, M., Pape, T., Bergès, B., dos Santos Fereirra, C., Boelmann, J., Geprägs, P., Tomczyk, M., Nowald, N., and Dimmler, W., 2014, Gas emissions at the continental margin west off Svalbard: mapping, sampling, and quantification: Biogeosciences Discussions, v. 11, p. 7189-7234.

Schöne, B. R., and Giere, O., 2005, Growth increments and stable isotope variation in shells of the deep-sea hydrothermal vent bivalve mollusk Bathymodiolus brevior from the North Fiji Basin, Pacific Ocean: Deep Sea Research Part I: Oceanographic Research Papers, v. 52, no. 10, p. 1896-1910.

Smith, A. J., Mienert, J., Bunz, S., and Greinert, J., 2014, Thermogenic methane injection via bubble transport into the upper Arctic Ocean from the hydrate-charged Vestnesa Ridge, Svalbard: Geochemistry Geophysics Geosystems, v. 15, no. 5, p. 1945-1959.

Snyder, G. T., Hiruta, A., Matsurnoto, R., Dickens, G. R., Tomaru, H., Takeuchi, R., Komatsubara, J., Ishida, Y., and Yu, H., 2007, Pore water profiles and authigenic mineralization in shallow marine sediments above the methane-charged system on Umitaka Spur, Japan Sea: Deep-Sea Research Part Ii-Topical Studies in Oceanography, v. 54, no. 11-13, p. 1216-1239.

Solomon, E. A., Kastner, M., Jannasch, H., Robertson, G., and Weinstein, Y., 2008, Dynamic fluid flow and chemical fluxes associated with a seafloor gas hydrate deposit on the northern Gulf of Mexico slope: Earth and Planetary Science Letters, v. 270, no. 1, p. 95-105.

Sommer, S., Pfannkuche, O., Linke, P., Luff, R., Greinert, J., Drews, M., Gubsch, S., Pieper, M., Poser, M., and Viergutz, T., 2006, Efficiency of the benthic filter: Biological control of the emission of dissolved methane from sediments containing shallow gas hydrates at Hydrate Ridge: Global Biogeochemical Cycles, v. 20, no. 2, p. GB2019.

Steefel, C. I., 2009, CrunchFlow- Software for Modeling Multicomponent Reactive Flow and Transport: User's Manual.

Sun, X., and Turchyn, A. V., 2014, Significant contribution of authigenic carbonate to marine carbon burial: Nature Geoscience, v. 7, no. 3, p. 201-204.

Tamelander, T., Aubert, A. B., and Riser, C. W., 2012, Export stoichiometry and contribution of copepod faecal pellets to vertical flux of particulate organic carbon, nitrogen and phosphorus: Marine Ecology Progress Series, v. 459, p. 17-28.

Torres, M. E., Wallmann, K., Trehu, A. M., Bohrmann, G., Borowski, W. S., and Tomaru, H., 2004, Gas hydrate growth, methane transport, and chloride enrichment at the southern summit of Hydrate Ridge, Cascadia margin off Oregon: Earth and Planetary Science Letters, v. 226, no. 1-2, p. 225-241.

Treude, T., Boetius, A., Knittel, K., Wallmann, K., and Jorgensen, B. B., 2003, Anaerobic oxidation of methane above gas hydrates at Hydrate Ridge, NE Pacific Ocean: Marine Ecology-Progress Series, v. 264, p. 1-14.

Trotsyuk, V. Y., and Avilov, V., 1988, Disseminated flux of hydrocarbon gases from the sea bottom and a method of measuring it, *in* Proceedings Doklady Earth Science, Volume 291, p. 218-220.

Tryon, M. D., Brown, K. M., Torres, M. E., Trehu, A. M., McManus, J., and Collier, R. W., 1999, Measurements of transience and downward fluid flow near episodic methane gas vents, Hydrate Ridge, Cascadia: Geology, v. 27, no. 12, p. 1075-1078.

Tryon, M. D., Brown, K. M., and Torres, M. E., 2002, Fluid and chemical flux in and out of sediments hosting methane hydrate deposits on Hydrate Ridge, OR, II: Hydrological processes: Earth And Planetary Science Letters, v. 201, no. 3-4, p. 541-557.

Tryon, M. D., Henry, P., and Hilton, D. R., 2012, Quantifying submarine fluid seep activity along the North Anatolian Fault Zone in the Sea of Marmara: Marine Geology, v. 315, p. 15-28.

Van Daele, M., Cnudde, V., Duyck, P., Pino, M., Urrutia, R., and De Batist, M., 2014, Multidirectional, synchronously-triggered seismo-turbidites and debrites revealed by X-ray computed tomography (CT): Sedimentology, v. 61, no. 4, p. 861-880.

Veloso, M., Greinert, J., Mienert, J., and De Batist, M., 2015, A new methodology for quantifying bubble flow rates in deep water using splitbeam echosounders: Examples from the Arctic offshore NW-Svalbard: Limnology and Oceanography: Methods, v. 13, no. 6, p. 267-287.

Veloso, M., Mienert, J., De Batist, M., and Greinert, J., Methane flux estimation of a large seep area offshore Svalbard based on visual observations and inverse hydroacoustic modeling, *in* Proceedings EGU General Assembly Conference Abstracts2014, Volume 16, p. 13130.

von Rad, U., Rösch, H., Berner, U., Geyh, M., Marchig, V., and Schulz, H., 1996, Authigenic carbonates derived from oxidized methane vented from the Makran accretionary prism off Pakistan: Marine Geology, v. 136, no. 1, p. 55-77.

Wallmann, K., Aloisi, G., Haeckel, M., Obzhirov, A., Pavlova, G., and Tishchenko, P., 2006a, Kinetics of organic matter degradation, microbial methane generation, and gas hydrate formation in anoxic marine sediments: Geochimica et Cosmochimica Acta, v. 70, no. 15, p. 3905-3927.

Wallmann, K., Drews, M., Aloisi, G., and Bohrmann, G., 2006b, Methane discharge into the Black Sea and the global ocean via fluid flow through submarine mud volcanoes: Earth and Planetary Science Letters, v. 248, no. 1-2, p. 545-560.

Westbrook, G. K., Thatcher, K. E., Rohling, E. J., Piotrowski, A. M., Paelike, H., Osborne, A. H., Nisbet, E. G., Minshull, T. A., Lanoiselle, M., James, R. H., Huehnerbach, V., Green, D., Fisher, R. E., Crocker, A. J., Chabert, A., Bolton, C., Beszczynska-Moeller, A., Berndt, C., and Aquilina, A., 2009, Escape of methane gas from the seabed along the West Spitsbergen continental margin: Geophysical Research Letters, v. 36.

Zabel, M., and Schulz, H. D., 2001, Importance of submarine landslides for non-steady state conditions in pore water systems - lower Zaire (Congo) deep-sea fan: Marine Geology, v. 176, no. 1-4, p. 87-99.

Figure Captions

Figure 1: Geographic location and the chimney system of our study sites. (A) Map showing the regional bathymetry and the location of Vestnesa Ridge. (B) Detail bathymetry of E. Vestnesa Ridge and the location of the five study sites. (C) Seismic profile crossing one of the active pockmarks investigated showing a well-established chimney system beneath.

Figure 2: Profiles of key pore water species and results from the steady-state modeling. Our model estimates the rate of key reactions (as shown by the red dash lines) by fitting the measured pore water profiles (blue and green solid lines). The discrepancy between the observed and modeled profiles (the first 50-70 cm at the three active sites) is due to a short-term (< years) non-steady-state behavior of the system which is not considered by our steady-state model.

Figure 3: X-radiograph and visual description of cores from HH13-197, -199, -200, and -203. We did not observe any anomalous sedimentary feature that could be associated with any geological events (*e.g.,* slope failures, mass transport events), bioturbation and gas tubes.

Figure 4: (A&B) Illustration of the aqueous pump mechanism. (C) - (E) Simulation results of sulfate profiles for the downward fluid water on the three active sites. Red solid lines show the initial condition used in this simulation. Green solid lines show the best fit model results. Our model is only able to constrain the longest time (Dt) and smallest *Darcy* flux (q) required, as shown on the figures.

Figure 5: Model estimated phosphate concentration by POSCR for different length of time and the comparison with the observed profiles.

769 Figure 6: Comparison of AOM rates derived from our steady-state model with the global dataset
770 compiled by Regnier et al. (2011). We estimated the theoretical maximum AOM rate by
771 extrapolating our estimation from 4 sites to the point where the depth of SMTZ is 2 cm, the
772 shallowest SMTZ ever reported in the literatures (Treude et al., 2003; Wallmann et al., 2006b).

773

774 Figure 7: Schematic summary of the three methane removal processes and reactions we model.
775 The importance of these processes/reactions is a function of their proximity to the center of
776 pockmark as well as the time scale over which they operate.

777

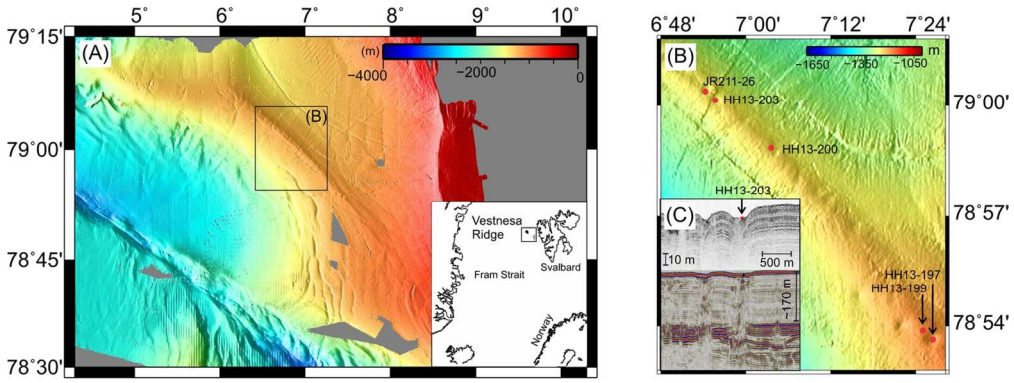

Figure 1: Geographic location and the chimney system of our study sites. (A) Map showing the regional bathymetry and the location of Vestnesa Ridge. (B) Detail bathymetry of E. Vestnesa Ridge and the location of the five study sites. (C) Seismic profile crossing one of the active pockmarks investigated showing a well-established chimney system beneath.
128x47mm (300 x 300 DPI)

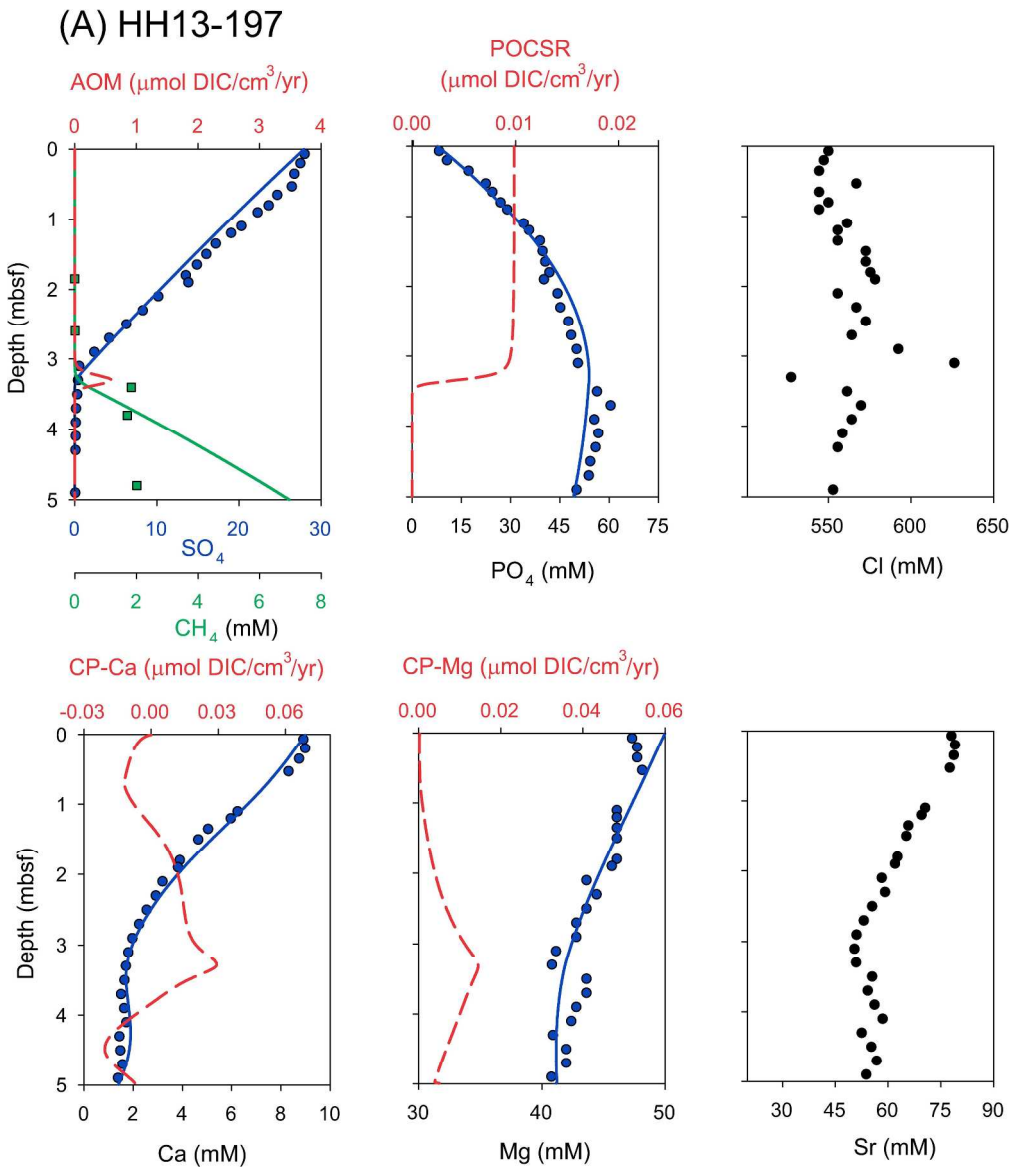

Figure 2: Profiles of key pore water species and results from the steady-state modeling. Our model estimates the rate of key reactions (as shown by the red dash lines) by fitting the measured pore water profiles (blue and green solid lines). The discrepancy between the observed and modeled profiles (the first 50-70 cm at the three active sites) is due to a short-term (< years) non-steady-state behavior of the system which is not considered by our steady-state model.
268x309mm (300 x 300 DPI)

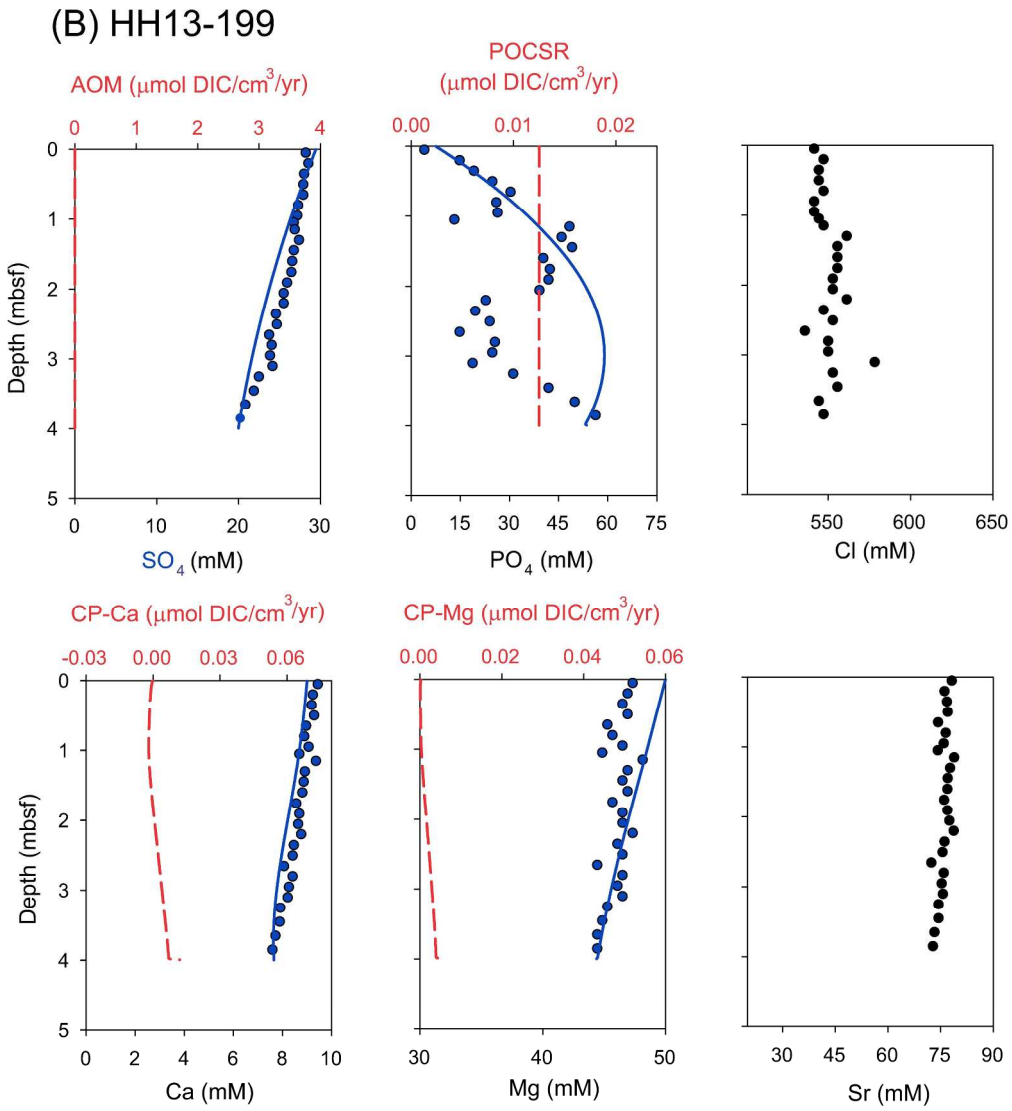

255x280mm (300 x 300 DPI)

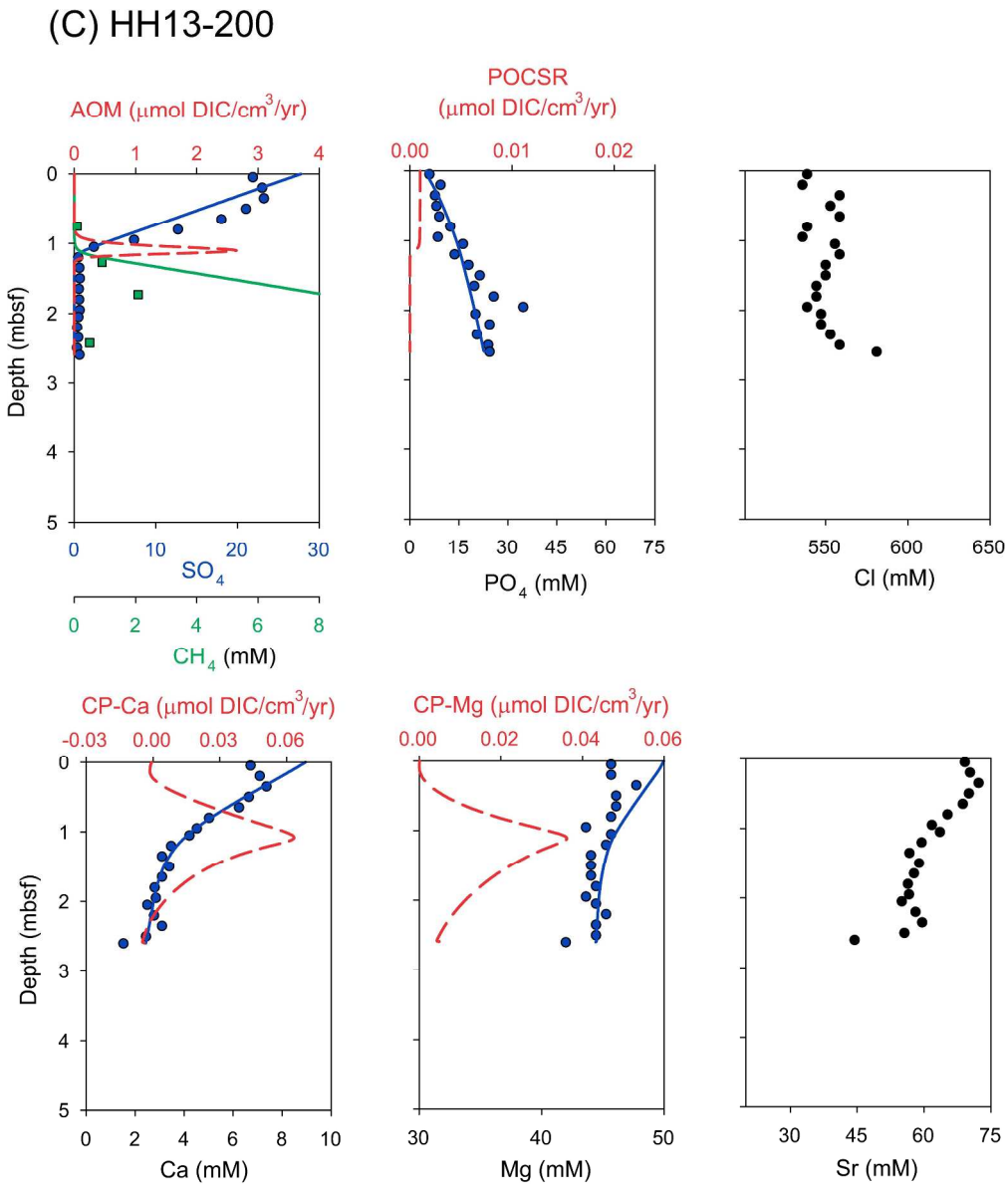

273x322mm (300 x 300 DPI)

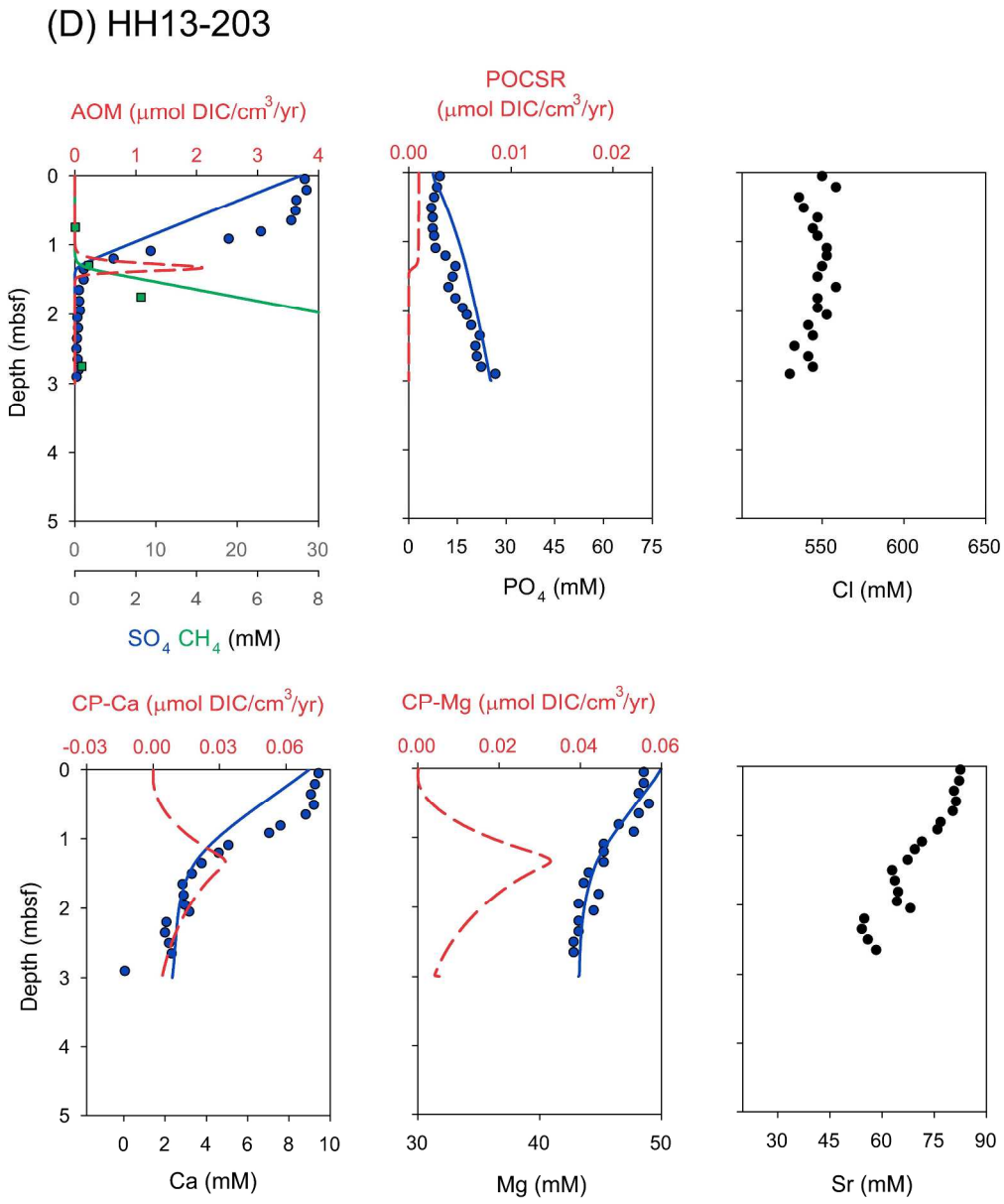

278x333mm (300 x 300 DPI)

(E) JR211-26

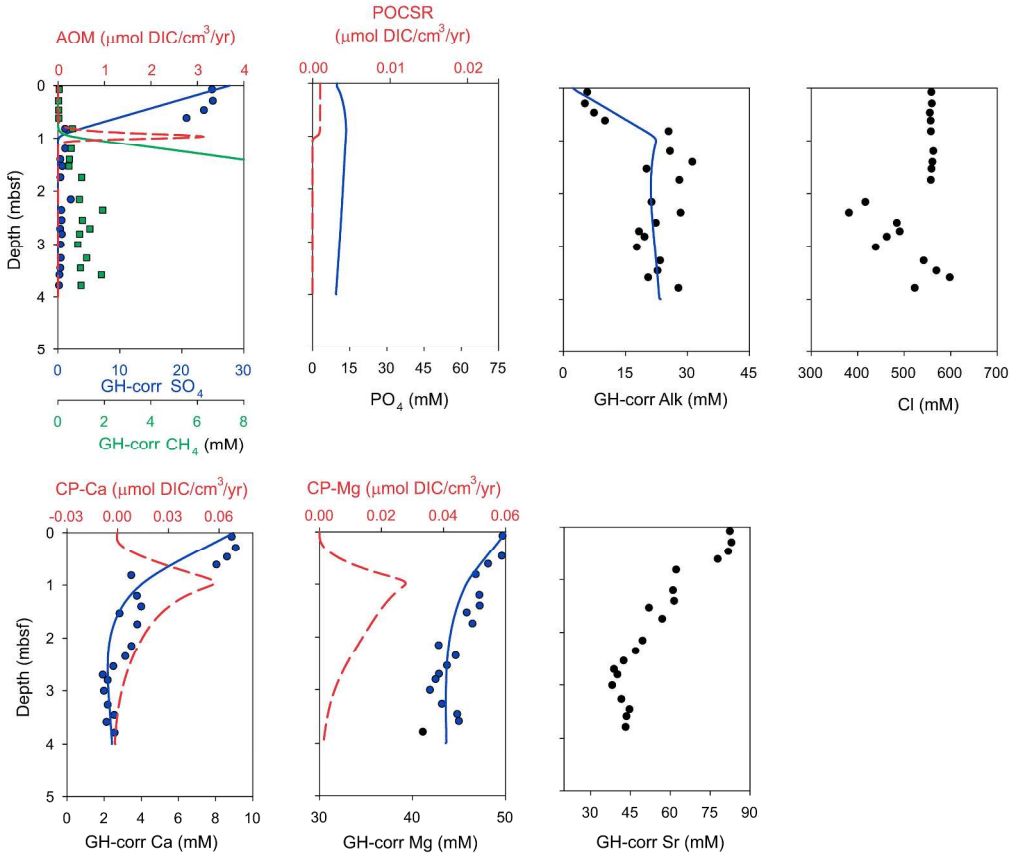

280x255mm (300 x 300 DPI)

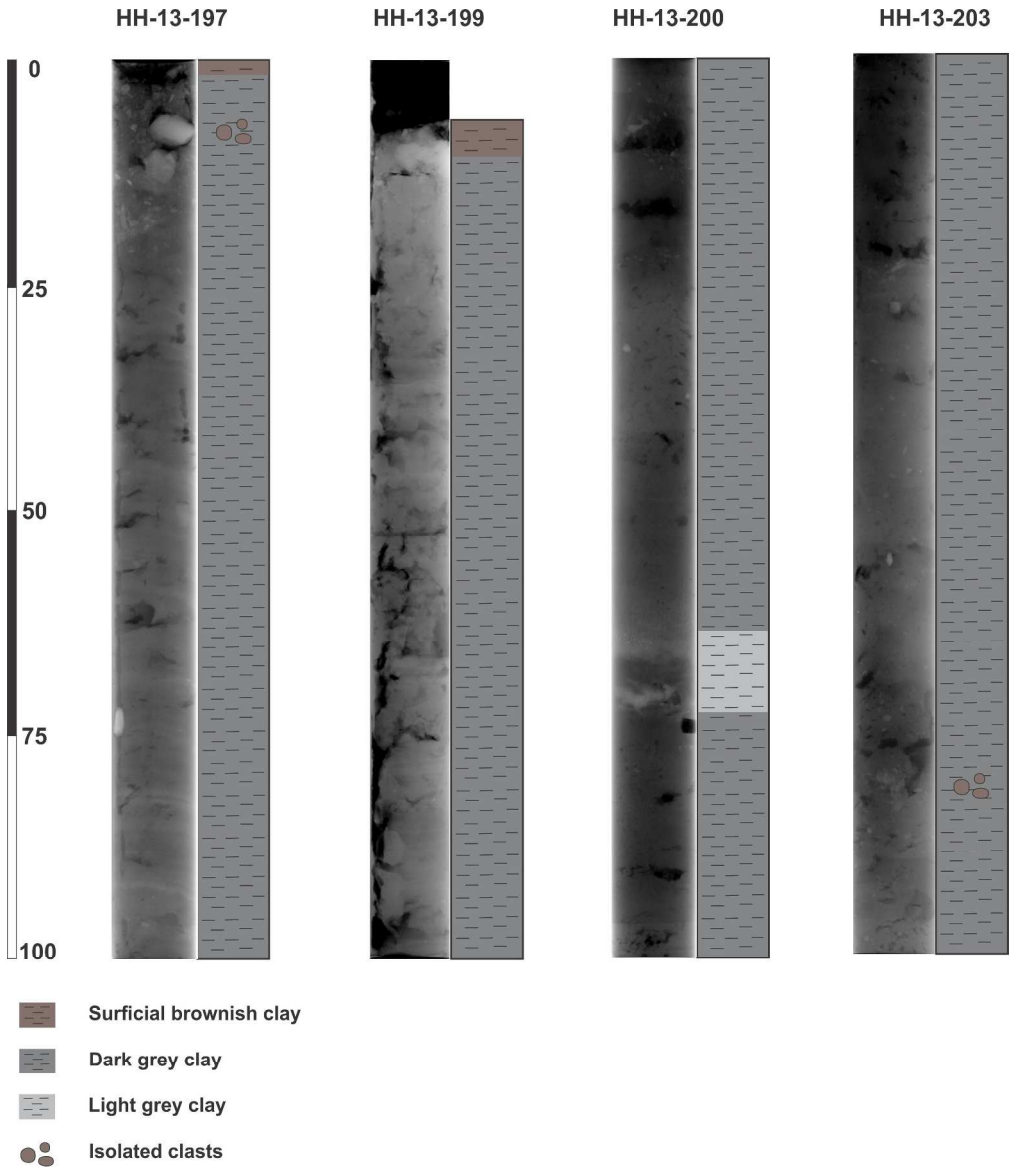

Figure 3: X-radiograph and visual description of cores from HH13-197, -199, -200, and -203. We did not observe any anomalous sedimentary feature that could be associated with any geological events (e.g., slope failures, mass transport events), bioturbation and gas tubes.
278x321mm (300 x 300 DPI)

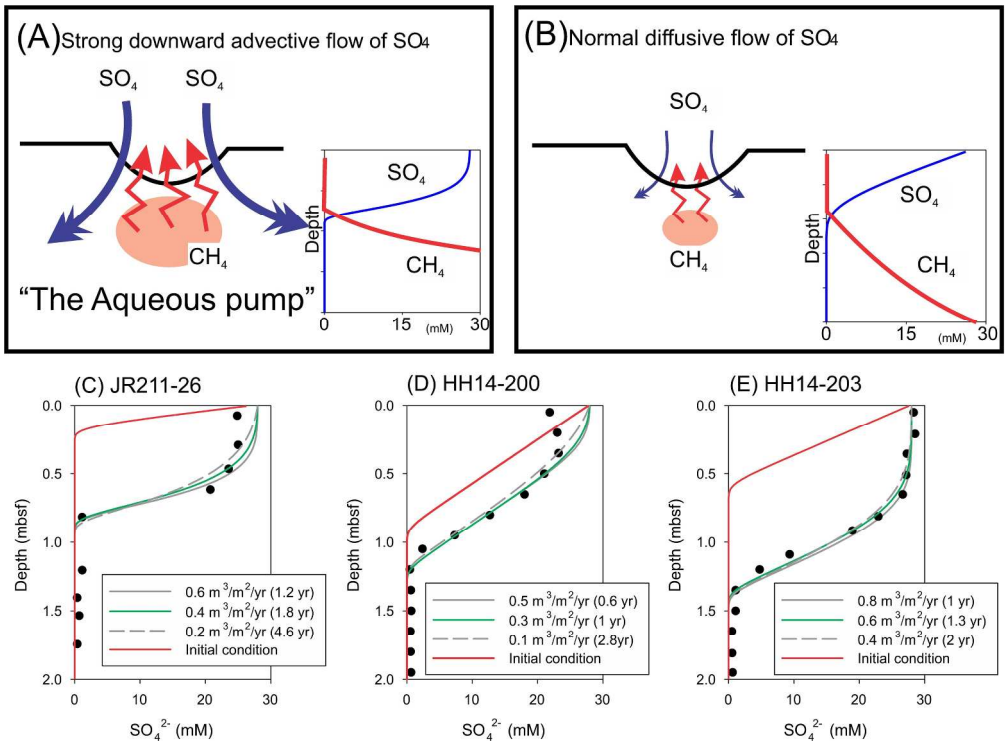

Figure 4: (A&B) Illustration of the aqueous pump mechanism. (C) - (E) Simulation results of sulfate profiles for the downward fluid water on the three active sites. Red solid lines show the initial condition used in this simulation. Green solid lines show the best fit model results. Our model is only able to constrain the longest time (Dt) and smallest Darcy flux (q) required, as shown on the figures.
241x177mm (300 x 300 DPI)

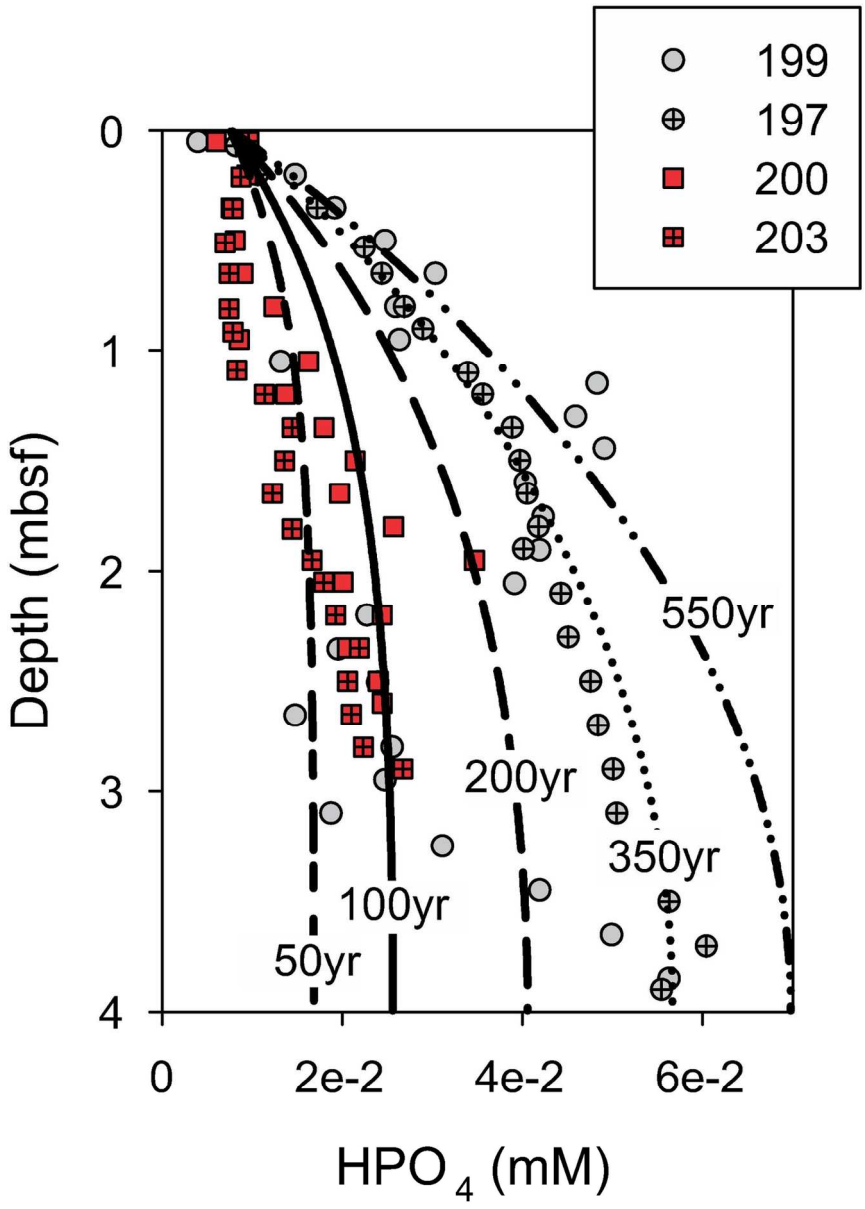

Figure 5: Model estimated phosphate concentration by POSCR for different length of time and the comparison with the observed profiles.
122x171mm (300 x 300 DPI)

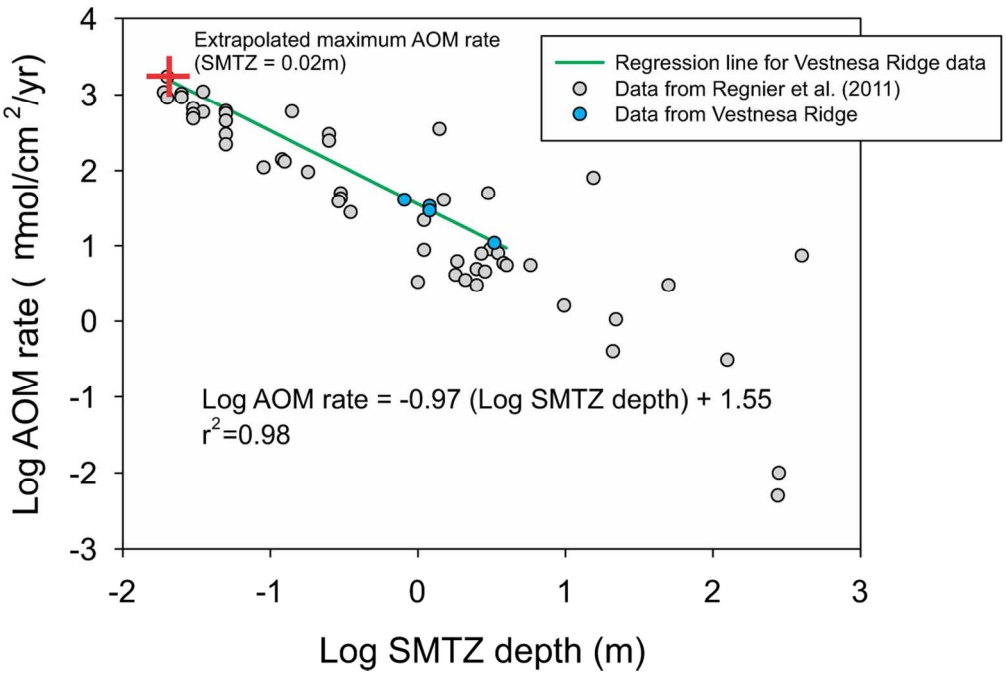

Figure 6: Comparison of AOM rates derived from our steady-state model with the global dataset compiled by Regnier et al. (2011). We estimated the theoretical maximum AOM rate by extrapolating our estimation from 4 sites to the point where the depth of SMTZ is 2 cm, the shallowest SMTZ ever reported in the literatures (Treude et al., 2003; Wallmann et al., 2006b).
112x74mm (300 x 300 DPI)

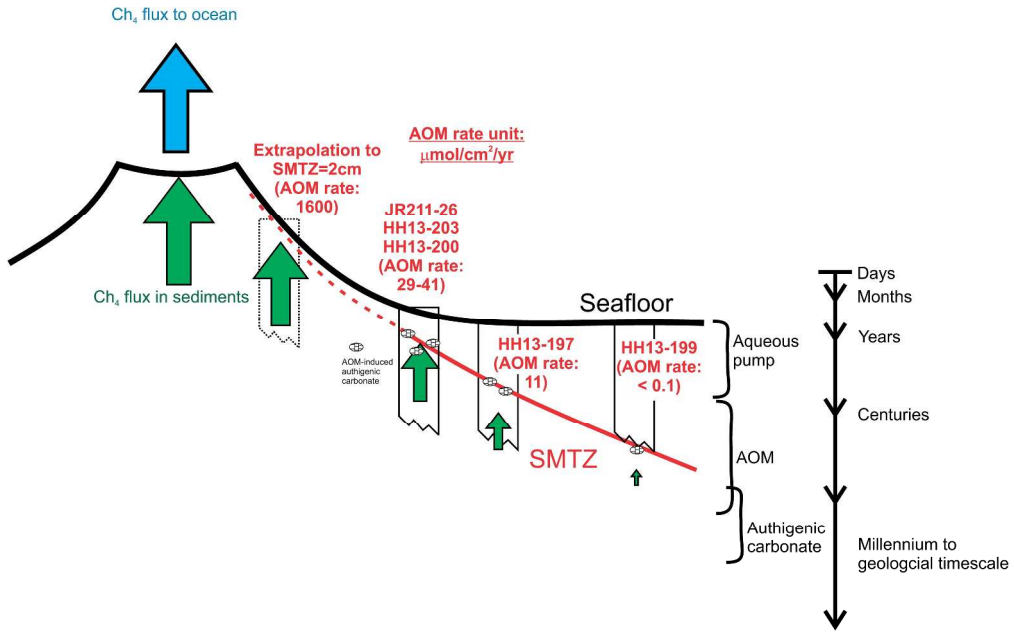

Figure 7: Schematic summary of the three methane removal processes and reactions we model. The importance of these processes/reactions is a function of their proximity to the center of pockmark as well as the time scale over which they operate.
314x196mm (300 x 300 DPI)

Table 1 Model-estimated Biogeochemical rates (μmol DIC/cm^2/yr)

	Water depth (m)	*SMTZ depth (m)*	*AOM*	*POCSR*	*CP-Ca*	*CP-Mg*	*Total SR*[1]	*AOM / Total SR*
HH13-197	1157	3.3	10.9	3.3	-0.9	-2.9	12.6	86.9%
HH13-199	1144	>3.85	0.08	5	-0.43	-0.63	2.6	3.0%
HH13-200	1205	1.2	33.7	1.2	-4.5	-3.8	34.0	99.1%
HH13-203	1198	1.2	29.3	0.9	-4.5	-3.9	29.6	99.3%
JR211-26	1210	0.8	40.9	1.0	-6.0	-4.1	41.4	98.8%

[1]Total SR = AOM+0.5 POCSR (μmol SO_4/cm^2/yr)

Table 2: Comparison of AOM rate and seafloor methane output with global datasets

	µmol $CH_4/cm^2/yr$	**Tons/year**	**References**
AOM rates			
a. Observed rates at Vestnesa Ridge	11 to 41	0.05 to 0.21 (radius=100m)	This study
b. Extrapolated rate at Vestnesa Ridge: SMTZ = 2 cm SMTZ = 0.2 cm	 1,600 140,000	 0.08 (r=10m) 7 (r=10m)	This study
c. Global model-derived rates	5E-3 to 1,720	2E-7 to 0.09 (r=10m) 2E-5 to 8.64 (r=100m)	Regnier et al. (2011) and the references therein
d. Global *in-situ* rates at seeps	37 to 2,044	2E-3 to 0.1 (r=10m) 0.18 to 10.3 (r=100m)	Boetius and Wenzhofer (2013) and the references therein
Seafloor methane output			
e. PKF hydroacoustic approach		187 to 250 144 to 1,888 220 to 347	Greinert et al. (2013) Sahling et al. (2014) Veloso et al. (2014)
f. Global *in-situ* benthic chamber measurements	110 to 44,749	6E-3 to 2.2 (r=10m) 6 to 225 (r=100m)	Boetius and Wenzhofer (2013) and the references therein

Supplementary material

Model numerical framework

POCSR rate was formulated as *Monod-type* rate expression with one *Monod* term and two inhibition terms:

$$R_{POCSR} = A_m k_m \exp[\frac{-Ea}{RT}]\prod a_i^n[1-\frac{Q}{K_{eq}}] \quad \text{(S1)}$$

$$k_m = k_{\max}^{POCSR}\left(\frac{C_{SO_4}}{C_{SO_4}+K_{half}}\right)\left(\frac{K_{in-HCO_3}}{C_{HCO_3}+K_{in}}\right)\left(\frac{K_{in-CH_4}}{C_{CH_4}+K_{in}}\right) \quad \text{(S2)}$$

where A_m (=1) and k_m are the surface area and kinetic constant. Ea, R, and T are the activation energy, ideal gas constant, and temperature. Πa_i^n is the activity product of solutes in the reaction with their stoichiometry (n) as exponents. $\frac{Q}{K_{eq}}$ determines the direction of reaction where Q is the ion activity product and K_{eq} is the equilibrium constant. As POCSR is a kinetic-driven reaction, we arbitrarily assigned a K_{eq} to ensure the reaction always in a forward direction. $k_{\max}^{POCSR}$ is the theoretical maximum rate that was obtained by fitting the observed pore water phosphate profiles at each site (Table S1). For JR211-26, where phosphate data are not available, alkalinity profile was used to constrain the rate of POCSR. K_{half} is the half saturation constant (=100 μM; Wegener and Boetius, 2009), and C_{SO4} is the concentration of sulfate. POCSR is inhibited by th accumulation of dissolved inorganic carbon and methane (Wallmann et al., 2006). We assumed inhibition constants (K_{in-HCO_3} and K_{in-CH_4}) are 20 mM based on the values proposed in Wallmann et al. (2006).

AOM was formulated as a *Monod-type* reaction with two *Monod* terms:

$$R_{AOM} = k_{\max}^{AOM}\left(\frac{C_{SO_4}}{C_{SO_4}+K_{half-SO_4}}\right)\left(\frac{C_{CH_4}}{C_{CH_4}+K_{half-CH_4}}\right)\left(1-\frac{Q}{K_{eq}}\right) \quad \text{(S3)}$$

where C is the concentration of electron donors or acceptors, Q is the ion activity product, $K_{half-SO_4}$ and $K_{half-CH_4}$ were set to be 500 μM (Wegener and Boetius, 2009) and 5 mM (Nauhaus et al., 2002; Vavilin, 2013), respectively. $k_{\max}^{AOM}$ was obtained by fitting the pore water profile and we assumed the same value for all sites (0.1 mol/kg water/yr). The equilibrium constant, K_{eq}, was calculated from the standard molar Gibbs free energy (G_f^0) of each reaction at 25 ^{o}C (values can be found in Hong et al. (2014)).

CP was formulated according to the *transition state theory* (Lasaga, 1981) (Eq. (S1)). The equilibrium constants (K_{eq} in Eq. (S1)) for the two carbonate phases are from the default database of CrunchFlow (Steefel, 2009) which use the same theoretical calculation from EQ3/EQ6, a software packages perform calculations of thermodynamics equilibrium for solution and mineral systems (Wolery, 1992) The kinetic constants, k_m^{Ca} and k_m^{Mg} (equivalent to the k_m in Eq. (S1)), for both CP were obtained by fitting the respective pore water profiles and reported in Table S1.

We developed a MATLAB routine to simulate the fluid advection in the shallow sediments from sites HH13-200, HH13-203, and JR211-26. This routine is coupled with CrunchFlow so that the biogeochemical reactions and diffusion can also be considered. Advection of fluid can be described as:

$$\frac{\partial C}{\partial t} = -v\frac{\partial C}{\partial x} \quad \text{(S4)}$$

where C is the concentration of solutes in the pore water (mole/m^3), t is time (yr), x is distance (m), and v is fluid velocity (m/yr). After discretizing space (Δx) and time (Δt), Eq. (S4) can be reformulated with an upwind explicit finite difference scheme:

$$C_x^{t+\Delta t} = C_x^t + \frac{\Delta t}{\Delta x}(v_x C_{x-\Delta x}^t - v_{x+\Delta x} C_x^t) \quad \text{(S5)}$$

We discretized the model time regime to small segments (Δt) and simulate fluid advection at each Δt. Simulations of diffusion and reactions by CrunchFlow were done for each time segment equivalent to $10\Delta t$, a frequency that was chosen to minimize the computing time (see later section for sensitivity test). The space discretization (Δx) in our MATLAB routine was determined by the magnitude of Δt and v following the *Courant-Friedrichs-Lewy* (CFL) condition:

$$\Delta t = CFL_{\max}(\frac{\Delta x}{v}) \quad \text{(S6)}$$

where CFL_{max} is the maximum allowed CFL value for numerical stability. For the explicit method, CFL_{max} should be 1 to maintain numerically stability and minimize numerical dispersion. We tested our simulation with progressively smaller Δt until a numerically stable solution was achieved. See later section for the criteria we used to determine Δt. The final length of time required for the assigned advective flow to reproduce the observed pore water profiles was estimated by integrating Δt to the desired time length (Dt).

The initial and boundary conditions

For both models, the observed core-top and bottom pore water compositions are used for boundary conditions (Table S1). For methane, we adjusted its concentration at the bottom of our model domain (Table S1) until the depth of the modeled SMTZ matches the observed depth. The

steady-state model was initiated with the observed core-top pore water composition at each site (Table S1). For the model quantifying the non-steady state condition in the shallow pore water system, we initiate the model with a well-defined SMTZ that is shallower than the one observed (Figure S1). The depth of this SMTZ is defined by the slope of the observed sulfate profile below the kinked depth at each site (~50-70 cmbsf, Figure S1).

Other essential model parameters

The depth discretization in both models is 1 cm. A total 260 to 500 cells are simulated for 14 kyrs, the bottom age of a core recovered north of our study sites (Consolaro et al., 2015). This age is younger than that reported for JR211-26 (Panieri et al., 2014), but is sufficient for the pore water system to reach steady state. Our measurements show that porosity remains constant (~0.68) for the first ~5m of the core, indicating no significant compaction within this depth range. The 25 ^{o}C diffusion coefficients for all pore water species are from Berner (1980) and Li and Gregory (1974). Diffusion coefficients were corrected for temperature, porosity and tortuosity to account for the slower diffusion in porous media under cold bottom water temperature (~-0.9 ^{o}C, Ferré et al. (2012)). CrunchFlow requires input of a cementation exponent to account for the tortuous flow in the porous media. As there is no information such as tortuosity or formation factor available for the Vestnesa Ridge sediments, we estimated the cementation exponent from a general relationship between porosity and formation factor reported by Berner (1980). Dependence of temperature is accounted for by assigning the activation energy in CrunchFlow. We fit the 0 ^{o}C and 25 ^{o}C measurements by Li and Gregory (1974) and obtained a value 5.6×10^{-25} kcal/mol for this activation energy input.

CrunchFlow numerical issue in advection

We did not use the CrunchFlow built-in function to describe fluid advection due to a significant numerical dispersion in CrunchFlow. This numerical issue is confirmed both by CrunchFlow developer (Steefel, personal communication) and also the tests we performed. Here we compared two simulations done by the CrunchFlow built-in function for advection (the “Erosion/burial” function) and our MATLAB routine to demonstrate such numerical issue. Both simulations were

done assuming a 4-meter sediment column. Constant porosity of 0.68 throughout the core was used. We turned off all reactions and diffusion; only advection of fluid is allowed. Fixed concentrations for the upper boundary condition was used; a no flux lower boundary condition was adopted. Three length of simulation time were chose: 20, 80 and 140 years. The maximum allowed time step in CrunchFlow was set to be 0.02 year. An even smaller time step (0.002 year) was used for the CrunchFlow simulation but no noticeable difference in results was observed. For the MATLAB routine, advection is evaluated every 0.2 years, a smaller time step is possible with longer computing time. A same *Darcy* velocity 0.01 $m^3/m^2/yr$ (or 0.0147 m/yr for fluid velocity assuming 0.68 porosity) was used in both simulations. Two cases were simulated: a fluid with high concentration of chloride advects downward (Figure S2A) and a high chloride concentration pulse being transported by the advected fluid (Figure S2B).

It is obvious from Figure S2A that the advection simulation done by CrunchFlow shows significant numerical dispersion as the edges of the square function are gradually smeared with time. On the contrary, the square functions were better preserved in the simulations done by the MTALAB routine. In the other case, where a pulse of Cl-rich fluid is transported by the advected fluid (Figure S2B), the peak heights in the simulations done by CrunchFlow were reduced by 9.7%, 18%, and 20% comparing to the original peak height. For the simulations done by MATLAB, the peak heights were only 3.6% reduced at most after simulating the flow for 140 years. The reduced peak height and gradually spreading peak are clear characteristics of numerical dispersion during the simulation of advection. This comparison justifies our decision not to use the built-in function of CrunchFlow to simulate advection. Our MATLAB routine provides a more accurate and numerical stable alternative for this purpose.

Sensitivity test for coupling CrunchFlow with the MATLAB routine for advection flow simulation

As described by Eq. (S5), there are three parameters required to simulate the advective flow: time discretization (Δt), space discretization (Δx), and *Darcy* flux of water (q). These three parameters are additionally constrained by the *Courant-Friedrichs-Lewy* (CFL) condition as shown by Eq. (S6). We ran a series of simulations with various choices of Δt and q (Δx is determined

subsequently by the CFL constraint). We also tested the coupling frequency between the MATLAB routine and CrunchFlow, which was ultimately chosen to be one CrunchFlow run for every 10 simulations of advective flow (*i.e.*, 10 runs of MATLAB routine). The chosen values for the sensitivity tests were summarized in Table S2.

Length of Δt is the most important factor influencing the convergence of the model. We observed good convergence when Δt is smaller than 0.02 year (Figure S3). The coupling frequency between CrunchFlow and MATLAB does not significantly impact the results as long as Δt is small enough. We therefore use 0.02 year as Δt and evaluate the profile with CrunchFlow every ten MATLAB runs in our simulations.

References

Berner, R. A., 1980, Early Diagenesis. A Theoretical Approach., Princeton, N. J., Princeton University Press.

Consolaro, C., Rasmussen, T. L., Panieri, G., Mienert, J., Bünz, S., and Sztybor, K., 2014, Carbon isotope (δ13C) excursions suggest times of major methane release during the last 14 ka in Fram Strait, the deep-water gateway to the Arctic: Clim. Past Discuss., v. 10, no. 5, p. 4191-4227.

Ferré, B., Mienert, J., and Feseker, T., 2012, Ocean temperature variability for the past 60 years on the Norwegian-Svalbard margin influences gas hydrate stability on human time scales: Journal of Geophysical Research: Oceans, v. 117, no. C10, p. C10017.

Lasaga, A. C., 1981, Transition state theory: Reviews in Mineralogy and Geochemistry, v. 8, no. 1, p. 135-168.

Li, Y. H., and Gregory, S., 1974, Diffusion of Ions in Sea-water and in Deep-sea Sediments: Geochimica Et Cosmochimica Acta, v. 38, no. 5, p. 703-714.

Nauhaus, K., Boetius, A., Kruger, M., and Widdel, F., 2002, In vitro demonstration of anaerobic oxidation of methane coupled to sulphate reduction in sediment from a marine gas hydrate area: Environmental Microbiology, v. 4, no. 5, p. 296-305.

Panieri, G., James, R. H., Camerlenghi, A., Westbrook, G. K., Consolaro, C., Cacho, I., Cesari, V., and Cervera, C. S., 2014, Record of methane emissions from the West Svalbard continental margin during the last 23.500 yrs revealed by δ< sup> 13</sup> C of benthic foraminifera: Global and Planetary Change, v. 122, p. 151-160.

Steefel, C. I., 2009, CrunchFlow- Software for Modeling Multicomponent Reactive Flow and Transport: User's Manual.

Vavilin, V., 2013, Estimating changes of isotopic fractionation based on chemical kinetics and microbial dynamics during anaerobic methane oxidation: apparent zero-and first-order kinetics at high and low initial methane concentrations: Antonie van Leeuwenhoek, v. 103,

no. 2, p. 375-383.
Wallmann, K., Aloisi, G., Haeckel, M., Obzhirov, A., Pavlova, G., and Tishchenko, P., 2006, Kinetics of organic matter degradation, microbial methane generation, and gas hydrate formation in anoxic marine sediments: Geochimica et Cosmochimica Acta, v. 70, no. 15, p. 3905-3927.
Wegener, G., and Boetius, A., 2009, An experimental study on short-term changes in the anaerobic oxidation of methane in response to varying methane and sulfate fluxes: Biogeosciences, v. 6, no. 5, p. 867-876.
Wolery, T. J., 1992, EQ3/6: A software package for geochemical modeling of aqueous systems: package overview and installation guide (version 7.0), Lawrence Livermore National Laboratory Livermore, CA.

181 Table S1 kinetic constants for various reactions considered in the model

		HH13-197	HH13-199	HH13-200	HH13-203	JR211-26
$k_{\max}^{POCSR}$		$10^{-9.5}$	$10^{-9.3}$	$10^{-9.8}$	10^{-10}	$10^{-9.5}$
k_m^{Ca}		$10^{-5.5}$	$10^{-6.5}$	$10^{-6.5}$	$10^{-6.5}$	10^{-7}
k_m^{Mg}		10^{-8}	10^{-8}	10^{-8}	10^{-8}	$10^{-8.5}$
Top boundary/ Initial condition	SO_4^{2-}	28 mM	28 mM	28 mM	28 mM	28 mM
	CH_4	~0 mM	~0 mM	~0 mM	~0 mM	~0 mM
	Ca^{2+}	9 mM	9 mM	9 mM	9 mM	9 mM
	Mg^{2+}	50 mM	50 mM	50 mM	50 mM	50 mM
	HPO_4^{2-}	7.5 μM	7.5 μM	5 μM	7.5 μM	7.5 μM
	Alk	2.2 mM	2.2 mM	2.2 mM	2.2 mM	2.2 mM
Bottom boundary condition	SO_4^{2-}	0 mM	20.2 mM	0 mM	0 mM	0 mM
	CH_4	7 mM	0 mM	20 mM	20 mM	50 mM
	Ca^{2+}	1.38 mM	7.58 mM	2.4 mM	2.32 mM	2.4 mM
	Mg^{2+}	40.77 mM	44 mM	44 mM	42.78 mM	43.17 mM
	HPO_4^{2-}	52 μM	56.27 μM	24 μM	26.7 μM	10 μM
	Alk	25 mM	25 mM	25 mM	25 mM	25 mM

182 Units are: k_{max} in mol/kg water/yr and, k_m in mol/m^2/sec

183

184

185 Table S2

Run#	Δt (yr)	Runtime in Crunchflow (yr)	Δx (m)	*v* (m/yr)
1	0.15	1.5	0.06	0.4
2	0.06	0.6	0.024	0.4
3	0.03	0.3	0.012	0.4
4	0.02	0.2	0.008	0.4
5	0.01	0.1	0.004	0.4
6	0.005	0.05	0.002	0.4
7	0.03	0.15	0.012	0.4
8	0.01	0.05	0.004	0.4
9	0.03	0.3	0.003	0.1
10	0.06	0.6	0.006	0.1
11	0.02	0.2	0.002	0.1
12	0.01	0.1	0.001	0.1
13	0.005	0.05	0.0005	0.1

186

187

188 Figure S1:Illustration of model progression with time

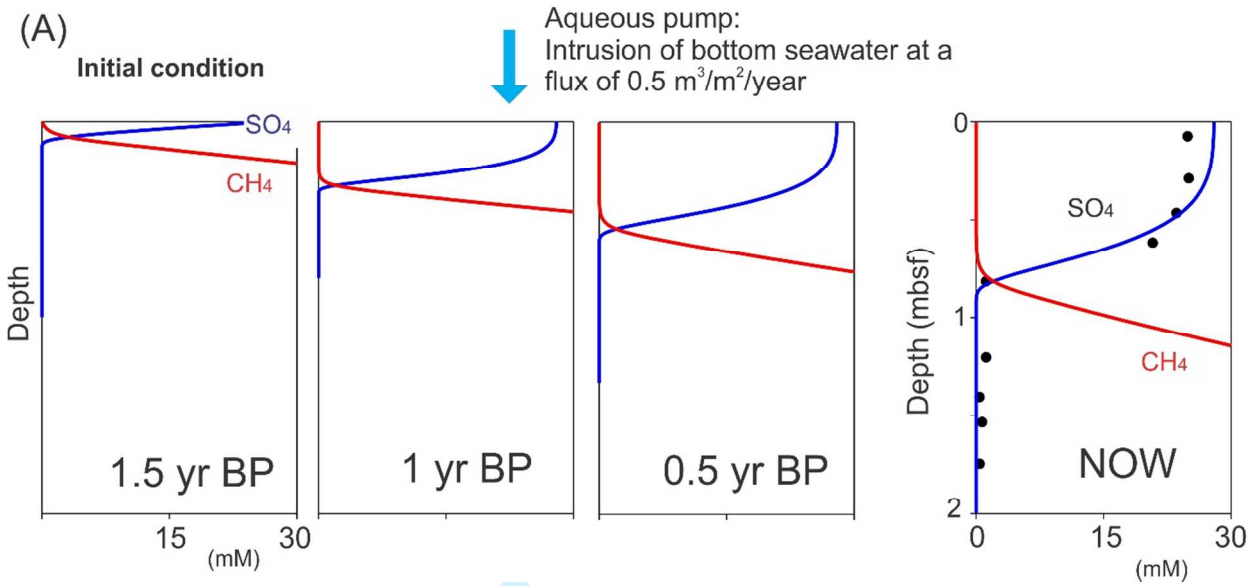

189

190

Figure S2: Comparison of fluid advection simulated by CrunchFlow built-in function and our MATLAB routine. Grey dash lines and blue solid lines are the results from CrunchFlow and our MATLAB routine, respectively. The red solid and dash lines in (B) mark the initial concentration of Cl. As we included only fluid advection in both models, there should be no concentration reduction during fluid transport. The reduction between the model results and the initial Cl concentration, as shown by the percentage, is solely due to numerical dispersion in both models. Our MATLAB routine provides more accurate model results with less numerical dispersion.

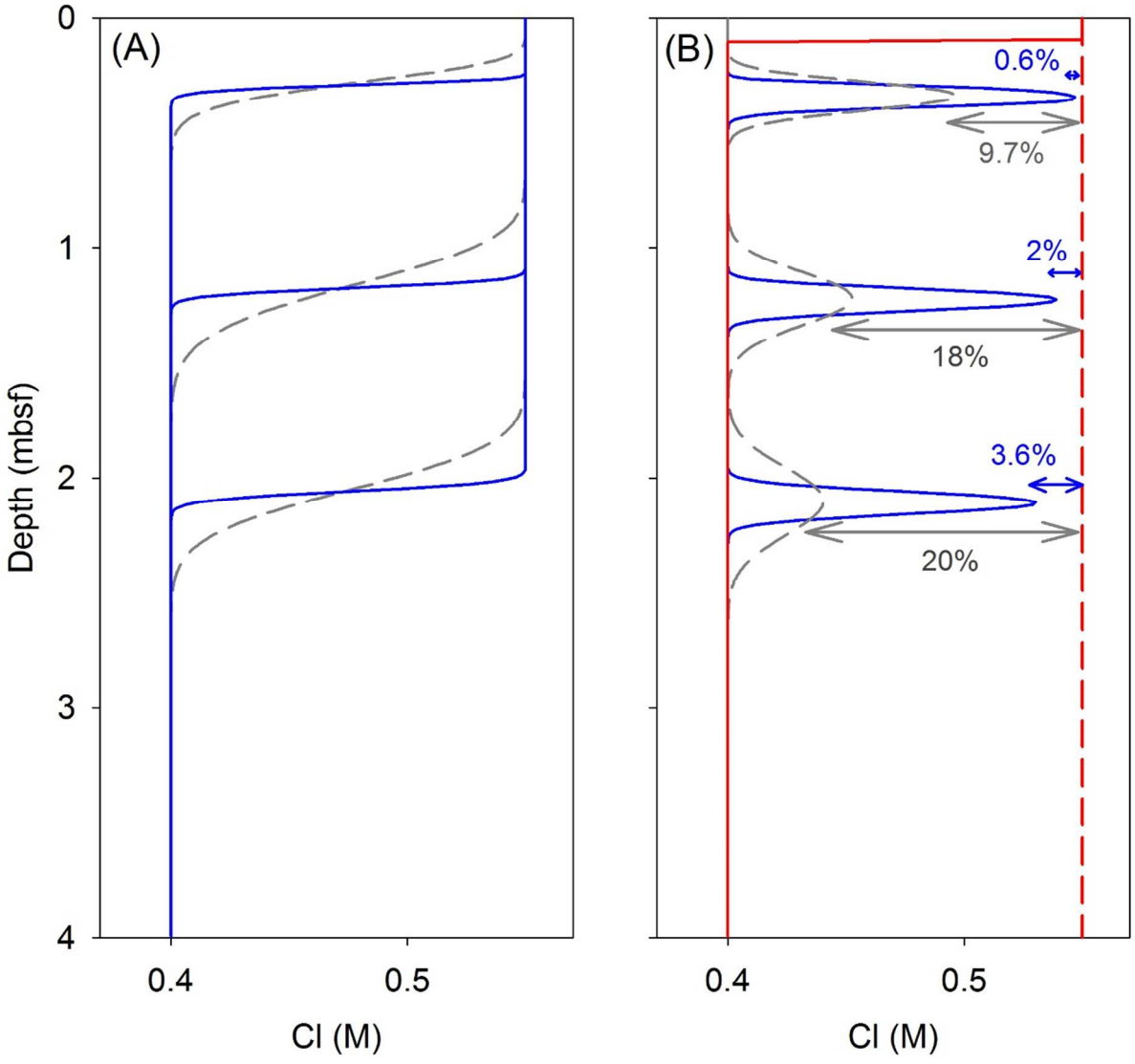

200 Figure S3: Sensitivity tests of our coupled model (CrunchFlow + MATLAB routine for fluid advection).
201 The values shown in (B) and (D) are time discretization (Δt), runtime in CrunchFlow, and Darcy velocity
202 for fluid (v). Parameters used for the sensitivity tests were included in Table S2.

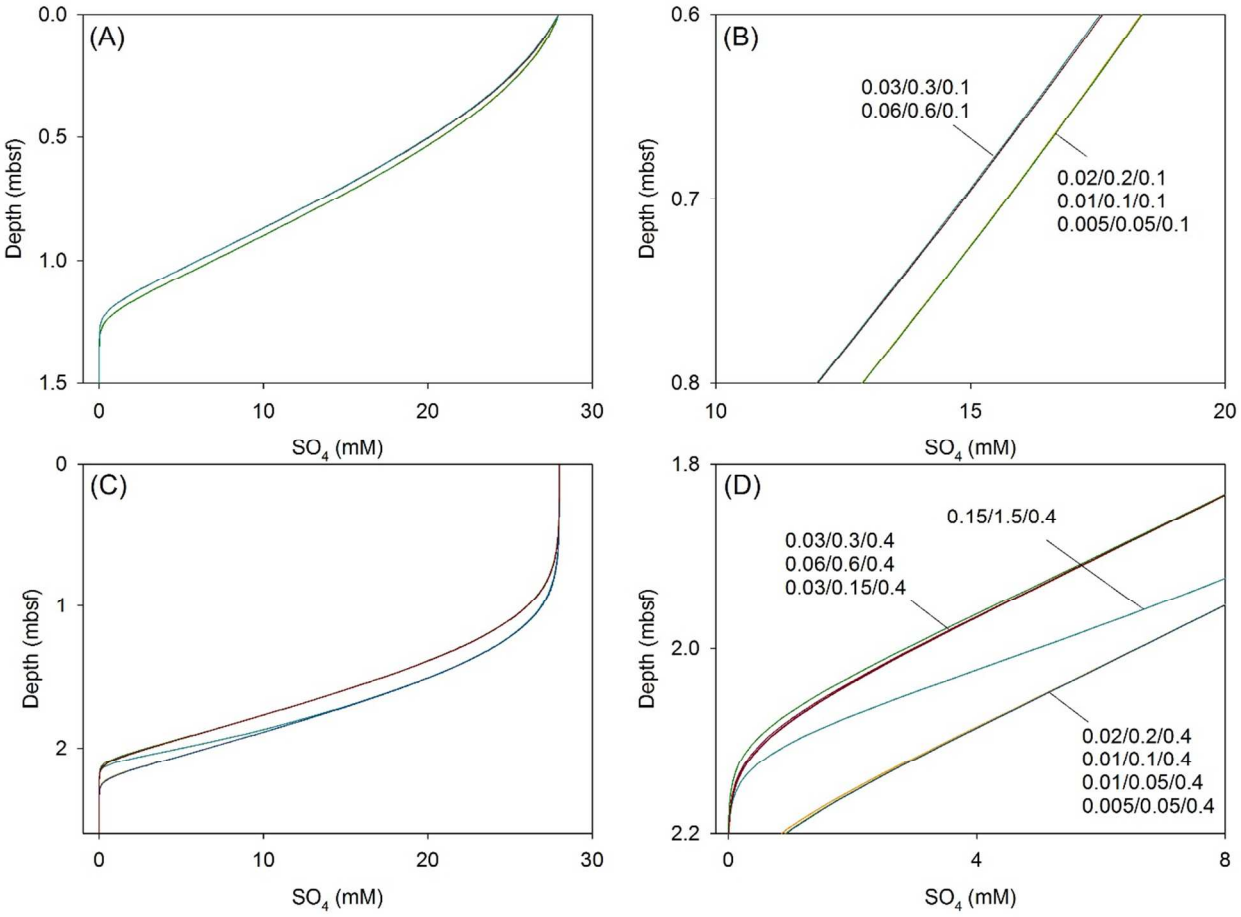

203

Review #1

The Manuscript ID LO-15-0348 entitled "Removal of methane though hydrological, microbial, and geochemical processes in the shallow sediments of pockmarks along eastern Vestnesa Ridge (Svalbard) is very interesting and provides the valuable information about methane turnover in the seepage sites in the Arctic region. This kind of dataset is relatively scarce and is worthy to publish after minor revision.

Major:

1) The MS mentioned three mechanisms for explaining the kinked porewater profiles. But there is other possibility of bubble irrigation was suggested by Haeckel et al. (2007) and Chuang et al. (2013), resulting in bottom water penetration. Both gas chimneys extending to the seafloor and acoustic flares in the water column have been observed, indicative of active methane bubble release at the seafloor. So the bottom water penetration down to 50-70 cmbsf may be due to bubbles release through the soft surface sediments instead of the aqueous pumping.

We agree that bubble irrigation can produce the exact porewater profiles as we observed here since this process also introduces bottom seawater although by different mechanisms (eddy diffusion vs. advection). We however think bubble irrigation is a less probable process to explain the kinked porewater profiles comparing to the aqueous pumping in our case because, as described by Haeckel et al. (2007), to stimulate eddy diffusion that is strong enough to result in the seawater-like profile, a tube radius of 1cm is required. We however do not observe tube-like structures this size in our cores. Aqueous pumping, on the other hand, requires no physical distortion of the sediments as the bottom seawater is introduced by pressure imbalance. We add a paragraph (Line 251 to 256 in the new MS) to justify our choice of aqueous pumping over bubble irrigation.

2) Line 286-296. Although it is true that methane degassing is quite heterogeneous at cold seeps, but bubble release at the seafloor should not be fully excluded based on your porewater profiles and geophysical data. Actually, the measured SO4, Ca, Mg data could be satisfactorily fitted by taking into account the bubble irrigation and gas dissolution during upward transportation in a steady state modeling.

As our previous reply, the porewater profiles cannot really differentiate between the two processes, aqueous pumping and bubble irrigation, since both of them introduce bottom seawater. A better choice of coring sites with TV-guided device to target sediments with visible bubbles may resolve this. In this work, we come to the conclusion that aqueous pumping is the mechanism responsible

for the seawater-like profiles based on our observations of sediments and the locations of these cores.

3) Line 345-362. The organic matter degradation seems in the steady state and the phosphate differences between active and no active site are more likely to be related to the accumulation of DIC and CH4 in pore water, which inhibits the organic matter degradation (Wallmann et al. 2006). I doubt the usefulness of PO4 profiles in estimating the duration of organic matter degradation.
Indeed the accumulation of DIC and CH_4 will retard the rate of organic matter degradation as described by Wallmann et al. (2006). We implemented such an effect in our model (see Line17-20 in the Supplementary material and Line 205 to 207 in the new MS) and estimated new age based on the fitting of our PO_4 profiles. The new age estimations are 50 to 150 years longer at the non-active sites than what we estimated previously. At the active sites, due to the already low organic matter degradation rate, the new ages are not significantly different from our previous estimation. Our conclusion that AOM has been active for couple centuries at the active sites compared to the non-active ones is still valid.

4) The MS concluded that the methane-fueled AOM has been persistently active during the last 2-3 centuries at the three active pockmarks based on PO4 profiles, which seems to contradict to the estimated time duration of continuous downward flow of bottom water (only 1-1.8 yr).
In the modeling the PO4 was set to seawater value, suggesting that there is no sulfate-organic matter reaction. The modeling results show that there is a gap about 100yrs of no methane seeping, which could occurred anytime during pockmark activity.
We interpret the two model results as seeping activity of different frequencies. The non-steady state downward flow is probably a high frequency process that is highly variable and dependent on the seepage activity of the pockmarks. Our results from the steady state model, together with the time estimated from the phosphate profiles, represent the long-term geochemical cycling that maybe of century to millennium scale. We therefore do not think the two results contradict each other. A paragraph is dedicated to clarify this (Line 390 to 395 in new MS).

Regarding the time gap from the phosphate modeling, first of all, the 100yr gap is a conservative estimate as the phosphate concentration at the active sites are mostly less than what can be produced in 50 years (the long dash line in Figure 5). Furthermore, the 50-100 yrs. gap is perhaps the sum of many short-term gaps that occurred throughout the entire active period. It is very

unlikely to have interruptions between methane supply episodes for more than a few decades as organoclastic sulfate reduction will be in effect as soon as sulfate is available for reaction and therefore produces phosphate. We dedicate a new paragraph to clarify this (Line 383-388 in the new MS).

5) Figure 2b: why were the measured sulfate data not well fitted? Perhaps you need to tune certain parameter for the organoclastic sulfate reduction.
After decreasing the C/P ratio (from 112 to 100 which is still within the error), decreasing the POCSR kinetic constant (from $10^{-9.3}$ to $10^{-9.4}$), and increasing the top boundary condition of sulfate (from 28 to 29mM), the measured profile can be fitted better (see the new Figure2b).

6) The calculated results of methane release and removal are only depending on the dissolved methane, not free methane gases. It needs to make clear in the MS.
This was made clear in throughout the MS.

7) The dissolved methane concentration in free gas-hydrate-water system is higher than that in free gaswater system or hydrate-water system (Cao et al., A kinetic model for the methane hydrate precipitated from venting gas at cold seep sites at Hydrate Ridge, Cascadia margin, Oregon. Journal of Geophysical Research: Solid Earth, 2013, 118(9): 4669-4681). It needs to discuss.
This is discussed in the ms (see Line 300 to 306).

8) The results show that 25% to 29% of the methane carbon is ultimately fixed as authigenic carbonates at the active pockmarks. But the equilibrium constant of carbonate precipitation, Keq, set to be a default value in the calculation (P41). In fact carbonate precipitation was controlled by pH and other factors. Therefore, the different Keq should affect the calculated profile of DIC, Ca, and Mg in depth, it needs to evaluate the influence of Keq on results in studied area.
The equilibrium constants (Keq) of calcite minerals are defined as the product of pH and calcium or magnesium activities, which already take into account the pH of porewater. The Keq values in the database of CrunchFlow are originally from the software package EQ3/EQ6 which performs calculation of thermodynamics equilibrium for aqueous solution and mineral systems (Wolery, 1992). The equilibrium constants were derived theoretically by the software based on the pressure, temperature, and solution condition (e.g., ionic strength and ion activity). We agree that values of Keq will affect the final model results; however, as the values we used are well-defined, we find no

reason to use different values. We included a paragraph in the supplementary material to justify the use of Keq values (see line 35-37 in the Supplementary material).

9) The flux of pore water will affect the calculated sulfate profile. Why does the advection rate of pore water set to 0.01m/yr in the calculation? How influence of varied advection rate of pore water on the results?

We did not include an advection component in our steady-state model because, based on the calculation of Peclet number and the age of our sediments (Pe=10^{-2} to 10^{-1}), advection is of very little importance comparing to diffusion. The 0.01 m/yr. advection rate mentioned by the reviewer is only the value we used to demonstrate the numerical dispersion of CrunchFlow when simulating advection and how our MATLAB routine can effectively eliminated such dispersion. We clarify this in the new MS (line 184-186).

Minor:

1) I suggest adding "methane seep", "numerical modeling", and pockmarks along eastern Vestnesa Ridge to the Keywords.

We added the first two keywords as suggested. As our title already includes Vestnesa Ridge pockmarks, we feel unnecessary to include that as a key word.

2) A table listing all the parameters included in the model should be added either to the MS or Supplement.

This was already done in Table S1 in supplementary material

Editorial comments

1) Line 16: should be sediments instead of sediment

2) Line 23: I suggest using "upper" instead of top

3) Line 42: which is then partially removed from solution

4) Line 58: no study from Vestnesa Ridge has been conducted to quantify the efficiency.....

5) Line 67: I prefer using "release" to "output"

6) Line 106: should be "below the sea surface" instead of from the sea surface

7) Line 132: a space should be added between 15 and cm

9) Line 63: “We then employed numerical modeling of the pore water profiles”. Need to add “(see supplement)”

We modified the text accordingly.

Removal of methane though hydrological, microbial, and geochemical processes in the shallow sediments of pockmarks along eastern Vestnesa Ridge (Svalbard)

Wei-Li Hong[1], Simone Sauer[1,2], Giuliana Panieri[1], William G. Ambrose Jr.[1,3,4], Andreia Plaza-Faverola[1], and Andrea Schneider[1]

[1] CAGE - Centre for Arctic Gas Hydrate, Environment and Climate, Department of Geology, UiT The Arctic University of Norway, Tromsø, Norway

[2] Geological Survey of Norway (NGU), Trondheim, Norway

[3] Department of Biology, Bates College, Lewiston, Maine USA 04240

[4] National Science Foundation, Division of Polar Programs, Arlington, Va. 22203

Abstract

The recent discovery of methane seeps in the Arctic region ~~urges for~~requires a better understanding of the fate of methane in ~~shallow~~ marine sediments ~~from this region~~if we are to understand the contributions of methane to Arctic ecosystems and climate change. To ~~this aim~~further this goal, we analyze pore water data from five pockmarks along eastern Vestnesa Ridge, a sediment drift northwest of Svalbard, to quantify the consumption of dissolved methane in the ~~shallow~~ sediments 3-5 meters below seafloor. We use transport-reaction models to quantify the hydrology as well as the carbon mass balance in the sediments. Pore water profiles and our model results demonstrate that hydrological, microbial, and geochemical processes/reactions efficiently remove methane carbon from fluid over different time scales. We interpret the non-steady-state behavior of the first 50-70 cm of our pore water profiles from the active sites as an annual scale downward fluid flow due to a seepage-related pressure imbalance. Such downward flow dilutes the concentration of methane within this depth range. Our steady-state modeling confirms the efficiency of anaerobic oxidation of methane (AOM) in consuming dissolved methane in the upper~~top~~ 0.8 to 1.2 meter of sediments. Based on the phosphate profiles, we estimate that AOM at the active pockmarks may have been operating for the last two to ~~three~~ four centuries. Precipitation of authigenic carbonate removes a significant fraction of methane carbon from fluid. More than a quarter of the dissolved inorganic carbon produced by AOM is fixed as

authigenic carbonate in the sediments, a process that sequestrates methane carbon over geological time ~~scale~~.

Keywords: methane seep, numerical modeling, anaerobic oxidation of methane

Formatted: Font: Bold

Introduction

Pockmarks are crater-like surficial expressions of the underlying fluid and gas system (Hovland et al., 2002) that have been commonly observed on the seabed worldwide (Judd et al., 2002; Hovland et al., 2002). Estimates of global methane emission from continental shelf seeps, including pockmarks, indicate that 1.9 to 65 teragrams (Tg, 10^{12} g) of methane are being emitted annually (Trotsyuk and Avilov, 1988; Hovland and Judd, 1992; Judd et al., 2002). A fraction of this, 0.4 to 12.2 Tg, reaches the atmosphere every year and constitutes a significant portion of the global atmospheric methane emission from geological sources (3-34%, Judd et al., 2002). How much of this methane actually reaches the water column and/or atmosphere is largely determined by the efficiency of the sedimentary biology sink for methane, the "benthic filter" (Sommer et al., 2006; Boetius and Wenzhofer, 2013). Macrofauna and microbes turn methane into other dissolved ions through metabolic processes. For example, a significant fraction of methane produced in the sediments is transformed, through anaerobic oxidation of methane, to dissolved inorganic carbon (Boetius et al., 2000; Hinrichs and Boetius, 2003), which is then partially removed from solution by authigenic carbonate precipitation (von Rad et al., 1996; Luff et al., 2005; Hong et al., 2014b). Despite the surmised importance of these processes, their nature and magnitude are poorly understood (Boetius and Wenzhofer, 2013).

Along Vestnesa Ridge, northwest of Svalbard, pockmarks are commonly observed on the seafloor collocated with an underlying acoustic chimney system (Bünz et al., 2012; Petersen et al., 2010). These pockmarks contribute a significant amount of methane to the water column (Bünz et al., 2012; Smith et al., 2014). Seepage along the ridge is restricted to the eastern segment of Vestnesa Ridge (Figure 1A). The detailed 3D seismic mapping of Plaza-Faverola et al. (2015) showed the evolution of seepage for the last ~2.7 Ma. Panieri et al. (2014) and Consolaro et al. (2015) documented repeated methane emission events for the last <23 kyrs. based on the

anomalously negative carbon isotope excursions measured on benthic and planktonic foraminifera shells. Ambrose et al. (submitted) observed discrete shell beds from two sediment cores recovered in this area and suggested prolonged (*ca.* 1000 yrs.) seepage activity approximately 17 kyrs. ago. While the past and present activity of these pockmarks is well documented, no study from Vestnesa Ridge has been conducted to quantifyied the efficiency of sedimentary methane sinks.

To identify and quantify the various methane removal processes in the shallow sediments of Vestnesa Ridge, we measured the concentration of major ions in the -pore water from five gravity cores collected in this region. We then employed numerical modeling of the pore water profiles (see *Supplementary material*) that -characterized the exchange of carbon among anaerobic oxidation of methane (AOM), particulate organic matter sulfate reduction (POCSR), and authigenic carbonate precipitation (CP). We compared our model-derived rates with global datasets and estimations of methane ~~output~~ release from the seafloor to assess the significance of our estimates. Our results reveal differences in carbon mass balance between the active and inactive pockmarks and confirm the importance of various processes/reactions in removing methane carbon from the shallow sediments along the eastern Vestnesa Ridge.

Formatted: Font: Italic

Geological Background

Vestnesa Ridge is a sedimentary drift developed under the effect of bottom currents along the west-Svalbard margin (Eiken and Hinz, 1993 and Howe et al., 2008). Despite its location on a passive margin, Vestnesa Ridge is in close proximity to active oceanic spreading ridges of Fram Strait (*e.g.,* Johnson et al., 2015) and geothermal gradients along the ridge are thus significantly higher than towards the passive margin (Crane et al., 1991). The sedimentary body consists of three main stratigraphic sequences that can be identified from seismic stratigraphy (Eiken and Hinz, 1993). The youngest sequence, YP3, is dominated by a long-slope transport and deposition from bottom currents with a major circular depocenter observed on the western Vestnesa segment (Eiken and Hinz, 1993). The middle sequence, YP2, has a depocenter parallel to the west-Svalbard margin that suggests a successive westward migration from Prins Karl Foreland (Eiken

and Hinz, 1993). The oldest sequence shows syn-rift and post-rift sedimentation on the < 19 Ma old oceanic crust (Engen et al., 2008; Johnson et al., 2015). Contourites, turbidites, and ice-rafted deposits have been commonly observed from sediments younger than mid-Weichselian on Vestnesa Ridge (Howe et al., 2008).

The Vestnesa Ridge gas hydrate system

Vestnesa Ridge hosts a deep water (> 1000 m) gas hydrate system characterized by a well-defined bottom simulating reflector (BSR) (Hustoft et al., 2009; Petersen et al., 2010). Gas hydrates have been recovered by gravity cores from some of the active pockmarks (Panieri et al., 2014; Smith et al., 2014). Seismic blanking that pierces through the gas hydrate stability zone (GHSZ) has been interpreted as gas-filled pathways. These are conduits for gas that migrates from deep hydrocarbon reservoirs toward the seafloor. Several of these gas chimneys terminate at the seabed below the observed pockmarks (Petersen et al., 2010; Bünz et al., 2012; Plaza-Faverola et al., 2015). It has been suggested that the eastern and western segments of Vestnesa Ridge are dominated by different tectonic stress fields that in turn affect the distribution and activity of seepage (Plaza-Faverola et al., 2015). We focus on three active pockmarks along the eastern Vestnesa segment (Figure 1) where gas chimneys developed along near-vertical NW-SE striking faults, interpreted as manifestation of shear deformation from the Spitsbergen Transform Fault (Plaza-Faverola et al., 2015). Abundant free gas below the GHSZ has been identified from seismic data (Hustoft et al., 2009; Figure 1C). Shallow gas accumulations as well as the presence of buried authigenic carbonate concretions and/gas hydrates at the interior of gas chimneys have been inferred by seismic anomalies in high resolution 3D seismic data (Plaza-Faverola et al., 2015). Acoustic flares detected by echosounder data from active pockmarks, extend as shallow as < 400 m below~~from~~ the sea surface, corresponding to the upper limit of the GHSZ for gas hydrates with thermogenic gases (Smith et al., 2014).

Analytical methods and results

We measured the concentration of major ions in the pore water from five gravity cores recovered along the eastern segment of Vestnesa Ridge during the 2008 RSS James Clark Ross (JR211)

cruise and 2013 R/V Helmer Hanssen cruise (HH13). Gravity cores were recovered from three active pockmarks with flares (JR211-26, HH13-200, and HH13-203), an inactive pockmark without a flare (HH13-197), and a background core *ca.* 200 m away from the nearest pockmark (HH13-199) (Figure 1B). Water depths of the five sites range from 1143 to 1210 meters (Table 1). Pore water sulfate and methane, which were measured from all five cores, are used to infer the depth of sulfate-methane-transition-zone (SMTZ) and estimate the strength of methane flux in the sediments. Pore water phosphate, a product of organic matter degradation, was measured from the four HH13 cores and used to infer pathways of organic matter turnover. Profiles of pore water calcium, magnesium, and strontium were determined from all five cores. These profiles reflect the rate of authigenic carbonate precipitation, an important carbon fixation pathway that turns dissolved carbon to carbonate minerals. The four HH13 cores were also examined using x-ray images to clarify the sedimentary sequence. We used GEOTEK X-ray core imaging system (MSCL-XCT 3.0) to image the archived half of the four HH13 cores. X-rays were made with an intensity of 120 keV and a resolution 20 mm. Before imaging, the archived spilt-cores were thawed in a cooling room. We dried the spilt-core surface with kimwipes and smoothed any obvious roughness to avoid interrupting the camera.

Pore water sampling and analyses for core JR211-26 were detailed in Panieri et al. (2014). For the other four sites (HH13-197, -199, -200, -203), cores were kept frozen onboard and brought back for shore-based analyses. After thawing the gravity cores in the cooling room (4°C), pore water samples were collected with rhizons (rhizon micro suction samplers: 10 cm, 0.15 µm porous polymer, Rhizosphere Research). We drilled 3.8 mm into the plastic liner at 15cm intervals and then inserted the wetted rhizons with 10 ml syringes attached. Wooden spacers were used to create a vacuum inside the syringes. The pore water collected was then filtered and diluted to proper ratios for analyses in Geological Survey of Norway (NGU) laboratories. We measured sulfate concentration by the Dionex ICS - 1100 Ion Cromatograph with a Dionex AS-DV autosampler and a Dionex IonPac AS23 column (eluent: 4.5 mM Na_2CO_3/0.8 mM $NaHCO_3$, flow: 1ml/min) and phosphate by spectrophotometry (Murphy and Riley, 1962). Prior to measuring for phosphate, concentrated HCl (10 µL) was added to 1 mL of pore water sample and left overnight to remove H_2S which will disturb the reaction forming the colour complex.

Ammonium molybdate solution (50 µL) and ascorbic acid solutions (50 µL) were well-mixed with 1mL of sample in a disposable polystyrene cuvette. After the treatment, samples were stored in the dark for ten minutes to complete the reaction. Concentration of phosphate was determined photometrically with a Shimadzu UVmini-1240 UV-Vis Spectrophotometer at a wavelength of 880 nm.

The pore water chloride profiles for all sites reflect no contribution from deep fluid (Figure 2). The low chloride concentration below 2 mbsf at JR211-26 (Figure 2E) reflects the influence from gas hydrate dissociation as hydrate was recovered below the corresponding depth. Concentrations of all pore water species, except for chloride, were corrected for this influence with correction factors (corr-F) defined as:

$$\text{corr-F} = [Cl^-]_{sample}/[Cl^-]_{avg} \quad (1)$$

where $[Cl^-]_{sample}$ is the measured chloride concentration with the influence of hydrate dissociation at each depth and $[Cl^-]_{avg}$ is the average chloride concentration for samples above 2 mbsf at this site (~558.6 mM), the samples that are free from the influence of gas hydrate dissociation.

For the three active pockmark sites (HH13-200, HH13-203, and JR211-26), the concentrations of all pore water species are constant and close to bottom seawater composition for the first 50-70 cm in the sediments and then decrease or increase rapidly (the "kinked" profiles hereafter) (Figures 2C, 2D, and 2E). The SMTZ is shallow at these three sites (0.8-1.2 mbsf, Table 1), compared to the other two sites (> 3 mbsf for HH13-197 and HH13-199, Figures 2A and 2B), suggesting a stronger methane flux at the active pockmarks. The kinked pore water profiles are clear signs of a non-steady-state condition that is due to recent and dynamic changes in either sediments or pore water (Zabel and Schulz, 2001; Hensen et al., 2003; Haeckel et al., 2007; Holstein and Wirtz, 2010; Hong et al., 2014a). Higher phosphate concentration for the non-active pockmark sites compared to active pockmarks is interpreted as faster organic matter degradation

rates and different sulfate reduction pathways. Rapid reduction in the concentrations of calcium, magnesium, and strontium from the three active pockmark sites indicates active authigenic carbonate precipitation that is promoted by the fast production of bicarbonate from AOM (Luff and Wallmann, 2003; Snyder et al., 2007; Wallmann et al., 2006a; Hong et al., 2014b). No authigenic carbonate, however, was observed.

The x-ray images and visual observation of the cores revealed mostly homogeneous dark or grey clay with occasional isolated clasts (Figure 3). Porosity was only measured at JR211-26. It is generally low and quite constant throughout the core (0.78 to 0.62; mean= 0.68, SD=0.03, n=19).

Model Setup

We developed two sets of models to quantify the biogeochemistry and hydrology in the sediments. In one set of models, we use CrunchFlow, a code designed to simulate solute diffusion and biogeochemical reactions (Steefel, 2009), to investigate and quantify the biogeochemical reactions under steady-state conditions. We included no advection component in this steady-state model as, based on the age of sediment (14 kyr, Consolaro et al., 2014) and the calculation of Péclet number (Pe=10^{-2} to 10^{-1}), advection is of very little importance compared to diffusion. We noticed non-steady-state behavior in the shallow part (<50-70 cm below seafloor) of the pore water system (see the *Results* section for more details). As a result, we further investigated this non-steady state behavior by coupling CrunchFlow with a MATLAB routine that we developed to simulate fluid advection. From the results of this modeling, we show that such non-steady-state was a short-term process and therefore does not undermine our assumption of steady state in the other model. We summarize the numerical framework of both models, the parameters used, and the boundary and initial conditions in the *Supplementary material*.

We consider three primary reactions in our model: particulate organic matter sulfate reduction (POCSR), anaerobic oxidation of methane (AOM), and authigenic carbonate precipitation (CP). Organic matter is consumed by sulfate (*i.e.*, POCSR) upon burial through microbial activities following the stoichiometry:

Formatted: Font: Italic
Formatted: Superscript
Formatted: Superscript

$$(CH_2O)(NH_3)_{\frac{19}{112}}(H_3PO_4)_{\frac{1}{112}} + 0.5SO_4^{2-} \rightarrow 0.5HS^- + 0.6516HCO_3^{2-} + 0.1695NH_4^+ + 0.008929HPO_4^{2-} + 0.3484CO_2 + 0.3484H_2O \quad (2)$$

We used 5.9 and 112 for C/N and C/P, respectively~~,~~; ratios obtained from sediment trap data at a location very close to our study sites with similar water depth (Tamelander et al., 2012). Accumulation of dissolved inorganic carbon (DIC) and methane inhibit organic matter degradation (Wallmann et al., 2006a). Such effects are considered in our model by implementing two inhibit terms (see *Supplementary material*).

Formatted: Font: Italic

A significant fraction of the pore water sulfate is consumed at the SMTZ through anaerobic oxidation of methane (AOM):

$$CH_{4(aq)} + SO_4^{2-} \rightarrow HCO_3^- + HS^- + H_2O \quad (3)$$

We assumed that all methane fueling AOM originates below our model regime, which accounts for any methane source that is located deeper than the sample depth. Methanogenesis from organic matter is excluded in our model domain, a choice justified by the small increase of phosphate concentration below the sulfate reduction zone (Figure 2).

Rapid AOM fueled by strong methane supply stimulates the precipitation of authigenic carbonate, which is obvious from the pore water calcium, magnesium, and strontium profiles (Figure 2). We included both Ca-calcite and Mg-calcite in the model to account for such observations:

227 $(Ca, Mg)\ CO_{3(s)} + H^+ \rightleftharpoons (Mg^{2+}, Ca^{2+}) + HCO_3^-$ (4)

228

229 To correctly account for the change of pH and alkalinity in the dissolved phase, we also included
230 different speciation of dissolved carbonate, ammonium, and phosphate. Dissolution of CO_2 and
231 CH_4 gases were also included although the model was set to be always water saturated (*i.e.,* no
232 gas phase transport). The full list of these secondary reactions and their respective equilibrium
233 constants are~~is~~ included in Hong et al. (2014).

234

235 **~~Model r~~Results and discussion**

236 *Quantifying the non-steady state condition of the pore water system*

237 Several processes have been proposed to explain kinked pore water profiles (Figure 2C to 2E): (1)
238 The sediment section with constant and near-seawater concentration may have been recently
239 deposited ~~-~~by mass movements of sediments, slumps, and/or slope failures (Zabel and Schulz,
240 2001; Hong et al., 2014a). Under this scenario, related sedimentary features such as complex
241 folding, crumpling, deformation structures, or imbricated mud clasts (Van Daele et al., 2014;
242 Baeten et al., 2014) should be observed in the sediments; (2) Exchange of bottom seawater by
243 infaunal animals or bioturbation. Animal burrows or traces from animal movements should be
244 evident~~-~~ in the sediments if bioturbation is important~~-~~ (O'Brien, 1987; Britt et al., 1992;
245 Löwemark and Werner, 2001; Rebesco et al., 2013); (3) Enhanced exchange between bottom
246 seawater and pore fluid due to irrigation by ascending methane bubbles from sub-seafloor
247 (Haeckel et al., 2007; Chuang et al., 2013); (4) Downward flow of bottom seawater into the
248 shallow sediments ("aqueous pump" hereafter) as proposed by Tryon et al. (1999). The aqueous
249 pump mechanism refers to the invasion of bottom seawater due to vigorous seeping of fluid in
250 adjacent sediments. Expelling of fluid from the adjacent sediments causes imbalance in hydraulic
251 pressure, especially in shallow sediments where sediments are not yet consolidated, and results in
252 bottom seawater invasion (Tryon et al., 1999; Figure 4A).

253

From the x-radiographs and our visual inspection (Figure 3), we observed no sedimentary features ~~related to either geological events or bioturbation.~~that can support the existence of geological events, bioturbation, and bubble irrigation. As concluded by Haeckel et al. (2007), to stimulate an eddy diffusion that is strong enough to result in the kinked porewater profile, a tube radius of 1 cm is required, which we did not observe during our visual inspection. Collectively, the aqueous pump mechanism is the most likely processes that can explain our observations from porewater profiles. The coincidence that the kinks are only obvious at the sites with shallow SMTZ (Figure 2C to 2E) suggests that these sites are closer to the center of active seepage, where methane flux is strongest, and therefore consistent with the postulate of an aqueous pumping mechanism.

From our simulation of fluid flow, we estimate the rate of fluid flow as well as the ~~-~~duration of aqueous pumping. We are only able to constrain the minimum value of fluid velocity and the largest time span for such downward fluid flow since diffusion tends to smooth the kinked pore water profiles if the advection term is too small. Our model estimates that, for the three pockmark sites, the aqueous pump has been operating for at most ~1 to 1.8 years (Figure 4C to 4E) and the minimum fluid flux required ranges from 0.6 to 0.3 m/yr. for the three sites. The resulting velocities are similar to what was measured in Hydrate Ridge (Tryon et al., 2002) and Gulf of Mexico (Solomon et al., 2008). We do not expect any distortion in the sediment structure under such low flow rate since the fluid velocity has to be a few orders of magnitude higher than our estimates to cause failure in sedimentary structure (Mörz et al., 2007).

Assuming the aqueous pump is associated with pockmark activity, the kinked pore water profiles reflect current activity that is no more than 1.8 years old. Few studies have ~~reported long term (> 1 year) monitoring of~~monitored seeping activity long term (>1 year). Solomon et al. (2008) monitored a seep site in the Gulf of Mexico with flow meters for more than 400 days. Tryon et al. (2012) deployed benthic chambers around seafloor venting in the Sea of Marmara for 13 months. Both records show pulses of strong fluid flow that ~~did~~ lasted for several months, which are in agreement with the duration we estimated from our pore water profiles. As the aqueous pump

process is a rather short-term process, it does not undermine our steady-state assumption for the carbon mass balance model.

Mass balance of carbon under steady state assumption

Based on the assumed biogeochemical reaction network, our model estimates the steady-state rates of AOM, POCSR, and CP. ~~Both the~~The rates of both POCSR and CP are constrained by the pore water profiles of phosphate, calcium, and magnesium. AOM rates thus equal the sulfate consumption not associated with POCSR. We integrated over the depth range for which the rate of each reaction is significantly higher than the background and express them as depth-integrated rates (Table 1). These rates were expressed as the amount of dissolved inorganic carbon (DIC, the sum of bicarbonate, carbonate, and dissolved CO_2) produced or consumed for comparison purposes. The rate of total SR is the overall sulfate reduction from AOM and POCSR. Methane flux from the bottom of our model regime can be inferred from the AOM rate as we included no other methane source in our model.

Our model results indicate a difference in carbon mass balance between the active pockmark sites and the non-active sites. AOM rates are 1 to 3 orders of magnitudes higher in the active sites than the non-active sites. There are ~~-~~only trace amounts of dissolved methane in the sulfate reduction zone (< 50 μM, Figure 2) from the active sites suggesting the rapid consumption of methane at the SMTZ. The pore water data, therefore, show that AOM in the sediment can effectively remove methane and prevent it from reaching ~~-~~the overlying seawater. The efficiency of AOM at removing dissolved methane from sediment is especially evident at JR211-26 where gas hydrate was recovered below 2 mbsf. To sustain such shallow gas hydrate reservoir, a kinetically-controlled gas-water-hydrate system is required (Torres et al., 2004; Liu and Flemings, 2006; Cao et al., 2013) which also implies potentially higher dissolved methane concentration compared to a system without free gas (Cao et al., 2013). It should be emphasized that~~,~~ even with such a shallow gas hydrate reservoir and potentially coexisting higher dissolved methane content, ~~virtually no methane escapes from the sediment at this site~~both AOM and aqueous pumping seal virtually all methane in the sediments at this site.

~~This~~ Such a result seems to contradict the general observations of acoustic flares in the water column along Vestnesa Ridge (*e.g.,* Bünz et al., 2012 and Smith et al., 2014). Seeping of gas bubbles in an area of a few m^2 or km^2 as revealed by echosounder surveys may be a common phenomenon in the area, but the spatial distribution of such degassing is in fact very heterogeneous. Seafloor observations of other cold seeps worldwide show that escaping of gas bubbles concentrate in an area of a few tens of cm^2 (*e.g.,* MacDonald et al., 1996; Haeckel et al., 2004; Nikolovska et al., 2008). The area surrounding sites of escaping gas shows no signs of degassing even though they may be close to a seeping center. It is likely that our cores with shallow SMTZ (*i.e.,* HH13-200, HH13-203, and JR211-26) were collected close to seeping centers but not directly over a site of degassing. Our pore water profiles and modeling show that AOM can effectively remove dissolved methane from the sediment when there is strong methane flux but not apparent degassing from the sea floor.

The strong methane fluxes and the resulting AOM stimulate 3 to 10 times more carbonate precipitation at the active sites than the other two sites with weaker methane fluxes (Table 1). The rapid production of bicarbonate by AOM is responsible for most of the CP rate differences between active and non-active sites. For the three active sites, methane carbon is transformed to DIC at a rate of 29.77 to 41.87 $\mu mol/cm^2/yr$. A significant fraction of this DIC production, 8.25 to 10.08 $\mu mol/cm^2/yr$ or 25 to 29% of the total AOM rate~~,~~ precipitates as authigenic carbonate by reacting with pore water calcium and magnesium. Such authigenic carbonate precipitation therefore serves as a very important sink for dissolved carbon in the sediments. The CP rates we estimated from the active pockmarks sites are similar to the rates estimated from Hydrate Ridge (115.5 $\mu mol\ DIC/cm^2/yr$; Luff and Wallmann, 2003) and an order of magnitude higher than the rates in Ulleung Basin (0.4-2.6 $\mu mol\ DIC/cm^2/yr$~~-~~; Hong et al., 2014b), Sea of Okhotsk (2.96 to -0.054 $\mu mol\ DIC/cm^2/yr$; Wallmann et al., 2006a), and Umitaka Spur (1.93 to 0.97 $\mu mol\ DIC/cm^2/yr$; Snyder et al., 2007; assuming the calcium and magnesium fluxes are equivalent to calcification rates). Our estimations also fall at the high end of the global range (Sun and Turchyn 2014)~~-~~. Such high CP rates should result in the accumulation authigenic carbonate in the sediments of active pockmarks along eastern Vestnesa Ridge. Panieri et al. (2014) documented

calcite overgrowth on the outside of foraminifera shells. ~~Such~~ This overgrowth has a depleted carbon isotopic signature compared to the biogenic tests and suggests a link with methane emission (Panieri et al., 2014). Ambrose et al. (submitted) also observed the presence of ~~micrite~~ carbonate concretions in the sediments from core HH 13-203. Although not from Vestnesa Ridge, Chow et al. (2000) reported detailed geochemical studies on the authigenic carbonate found from ODP Site 909, a site drilled a few kilometers south of Vestnesa Ridge. From the elemental composition of these Fe-Mn carbonates with enriched calcium and magnesium, Chow et al. (2000) suggested these carbonates might precipitate in the suboxic zone of sediments, from the Fe-reduction to the early methanogenesis zone.

The proportion of sulfate consumed by POCSR at the two non-active sites covers a wide range, from 13.1 to 97%, whereas almost all sulfate is consumed by AOM at the active sites (Table 1). At sites HH13-197 and -199, active POCSR lowers pH by adding CO_2 to the system (Eq. (2)) and therefore dissolves carbonate minerals. Authigenic carbonate precipitation was suppressed for the first meter at these two sites due to active POCSR over this depth (Figure 2A and 2B). The modeling done by Luff et al. (2001) and Jourabchi et al. (2005) also shows decreasing pH when organic matter degradation dominates.

Pore water phosphate as an indication of organic matter turnover

Contrasting levels of phosphate among sites (Figure 2) suggest different organic matter degradation rates and resulting sulfate reduction pathways. For sites with abundant methane supply (*i.e.,* shallow SMTZ), AOM is stimulated by the increasing methane supply from below. POCSR is less active under this condition as most sulfate reacts with methane through AOM. We account for this effect by using a small kinetic constant for POCSR in our steady-state simulation (Table S1 in *Supplementary material*). On the other hand, when the pockmark activity wanes, more sulfate is available for POCSR which results in the higher phosphate level observed from the inactive sites. We therefore need to use a larger kinetic constant to describe this scenario in our model.

If we assume the same organic matter composition (*i.e.,* similar reactiveness and C/P ratio) for all the study sites, the factor controlling the level of pore water phosphate is the time duration of organic matter degradation; *i.e.,* more phosphate is released when organic matter is degraded for a longer time. We modified our steady-state model to estimate how long organic matter has been degraded at the four HH13 sites. We used the kinetic constant from site HH13-199, a site that has minimum influence from AOM as we did not penetrate the sulfate reduction zone at this site with our 5-meter gravity core. AOM was inhibited in this model run and we used a no flux lower boundary condition assuming no input of phosphate below the model regime. We adopted these crude assumptions to provide a first-order estimation of the length of time that organic matter has been actively consumed by sulfate (*i.e.*, POCSR). The variation in C/P molar ratios (112±12) reported by Tamelander et al. (2015) results in a 25-year uncertainty in our age estimation. Our model suggests that it takes ~~300~~ 350 to ~~400~~ 550 years for POCSR to produce the amount of phosphate observed at sites HH13-197 and HH13-199 (Figure 5) and less than 50-100 years for sites HH13-200 and HH13-203 (Figure 5). The short POCSR effective time for the two active pockmark sites implies that most sulfate has *not* been consumed by POCSR. This model result therefore delivers an important message: most pore water sulfate at the two active pockmark sites was consumed by the methane-fueled AOM for the past approximately two to ~~three~~ four centuries. Methane flux has to be persistently strong during this time period. The 50-100 years gap at the two active sites when methane supply waned and sulfate was available for POCSR is probably the sum of many short-term gaps that occurred throughout the entire active periods. It is very unlikely to have interruptions between methane supply episodes for more than a few decades as organoclastic sulfate reduction will be in effect as soon as sulfate is available for reaction and therefore produces phosphate.

Together with the 1 to 1.8 years long aqueous pumping we estimated by modeling the kinked porewater profiles, we interpret both frequencies, year-long and centurial-scale, as seeping activities modulated by processes of different time scales. The aqueous pumping represents the short-term "breaths" of the pockmarks while the supply of methane, which may be related to the stress field at depth (Plaza-Faverola et al., 2015), can be several centuries long, as we estimated from the phosphate profiles.

Formatted: Font: (Default) Times New Roman, 12 pt, Font color: Auto

Ambrose et al. (submitted) observed a high concentration of bivalve shells and fragments spanning 30 cm (2.36-2.68 mbsf) in core HH13-203, the same core we investigated. The bivalves in this "clam bed" were dominated by two genera of the Vesiscoymidae which are dependent on sulfide-reducing endosymbioitc bacteria for nutrition (Krylova and Shaling, 2010). These bivalves, therefore, can only survive under conditions of persistent methane flux and the age of an individual bivalve is, therefore, an estimate of the minimum length of time of strong methane emission. By counting the number of rings in the hinge of one large individual (*Phreagena* s.l.), and assuming the lines to be annual the clam was estimated to be 20-25 years old (Ambrose unpublished data). Deep-sea bivalves that have been investigated are known to deposit daily growth lines apparently with a tidal rhythm (Schöne and Giere, 2005; Nedoncelle et al., 2013), but none have been investigated for annual lines so the age estimate is speculative. The clam bed in the core persisted for approximately 1000 years from 17,707 to 16,680 years ago. The 1000-year duration of seeping constrained by the presence of bivalves in the core is longer than, but similar to, the length of time ~~duration~~ we estimated based on the phosphate profiles (200-~~300~~ 400 years). This suggests that the site was subject to several seeping events in the past with events ranging in duration from a few centuries to a thousand years.

Fate of methane in Vestnesa Ridge sediments

The significance of AOM as an important dissolved methane sink has been widely appreciated for ~~-~~decades (Hinrichs and Boetius, 2003; Knittel and Boetius, 2009; Regnier et al., 2011; Boetius and Wenzhofer, 2013). Quantification of AOM rates by experiment or modeling techniques, however, has received far less attention (Knittel and Boetius, 2009; Regnier et al., 2011; Boetius and Wenzhofer, 2013). Our effort to quantify AOM along Vestnesa Ridge adds another estimate in the Arctic, where such estimates are scarce (Regnier et al., 2011). Comparing our estimates with the global model-derived AOM rates compiled by Regnier et al. (2011), our results fall in the center of the data cluster (Figure 6). Extrapolating from our four estimates (excluding HH13-199) to the point where the depth of SMTZ is only 2 cm, the shallowest SMTZ ever reported ~~in~~ from the Black Sea and Hydrate Ridge (Treude et al., 2003; Wallmann et al., 2006b), we can approximate the maximum AOM rate (1600 μmol/cm^2/yr, *b* in Table 2) at the near-center of

pockmarks from Vestnesa Ridge (Figure 7). This rate is likely to be even higher if the SMTZ is shallower than 2 cm (*b* in Table 2). The maximum AOM rate we estimate is in agreement with the highest model-derived rate (Regnier et al. 2011) and the highest *in-situ* rate ever reported in Hydrate Ridge (Treude et al., 2003; Boetius and Wenzhofer, 2013) (*c* and *d* in Table 2). The next question will be how does such a high ~~-~~AOM consumption rate compare with the output of methane from seafloor to water column.

Wide-spread acoustic flares have been well-documented along Vestnesa Ridge (*e.g.,* Bünz et al., 2012 and Smith et al., 2014) although no output of methane has yet, to the best of our knowledge, been quantified in this region. The estimations of methane output at Prins Karl Foreland (PKF), the shallow ~~-~~water seep sites west of Svalbard, suggest an output of more than 144 tons/year~~s~~ of methane (*e* in Table 2). It is likely that such methane output from PKF is higher than the output from the pockmarks along Vestnesa Ridge since PKF is considered to be more active due to its location (Westbrook et al., 2009; Berndt et al., 2014). The precise estimation of methane output in the water column of Vestnesa Ridge awaits future studies. By integrating the AOM rate we estimated over the area of the pockmark (assuming 10 meters or 100 meters radius), AOM consumes only 0.05 to 0.21 tons of methane annually, a small fraction of the output estimated from acoustic flares (*a* in Table 2).

The different estimation in AOM rates and escaping output of methane may be partly due to the uncertainties and limitations associated with both methods of measurements. Our extrapolation of the maximum methane consumption by AOM ~~very much~~ depends to a large extend on the depth of the SMTZ. The consumption increases ~100-fold when the depth of the SMTZ varies by a factor of 10 (*b* in Table 2). Such an increase in consumption is, however, counterbalanced by the smaller area covered by such focused consumption. ~~It is very likely t~~The annual rate of methane consumption is likely to be the ~~hat on the~~ order of 100 kg (0.1 tons) per year ~~of methane consumption per year~~which would be ~~is~~ the highest rate recorded globally (Regnier et al. 2011; Boetius and Wenzhofer 2013).

There are uncertainties in the hydroacoustic method for quantifying gas bubble flow rate (Veloso et al. 2015). By comparing the models from several investigators, Velosco et al. (2015) concluded that the relative error can be as much as 60%. Furthermore, in order to convert flow rate to methane output, one must know the concentration of methane in bubbles, a parameter that is assumed to be 100% methane in PKF based on the measurements done by Sahling et al. (2014) at one seep. This concentration may be temporally and spatially variable. Boetius and Wenzhofer (2013) compiled *in-situ* benthic chamber measurements that determine the flux of methane leaving surficial sediments from seeps worldwide. The flux ranges from several hundred to 44,749 μmol/cm^2/yr (*f* in Table 2). In order to arrive at an estimate similar to the values reported at PKF, we have to assume the highest flux seeping from an area with radius of 100 m (*f* in Table 2), which is an unreasonable assumption. It is beyond the scope of our paper to resolve the different estimations made by different methods. We note, however, the importance of such an exercise to comprehensively understand the fate of methane in sediments. Despite all the uncertainties, we may still conclude that AOM consumes a rather small fraction of methane in the Vestnesa Ridge surficial sediments compared to what escapes from the seafloor, although the exact fraction is still unclear.

Summary

Vestnesa Ridge has been confirmed by both the mapping of fluid pathways in the sediments and acoustic flares in the water column to be an area of high levels of methane seepage from the seafloor (Petersen et al., 2010; Bünz et al., 2012; Smith et al., 2014). The potential discharges of methane from geosphere to hydrosphere are nevertheless speculative (Bünz et al., 2012; Smith et al., 2014). The biological and chemical reactions at, or near, the sediment surface represent the last line of defense preventing dissolved methane from escaping the sediments. We model the efficiency of these processes in filtering methane at Vestnesa Ridge and show that dissolved methane in the shallow sediments (<5 mbsf) is consumed or diluted through hydrological, microbial, and geochemical processes/reactions (Figure 7).

- We attribute the kinked pore water profiles from the three active pockmark sites as the consequence of seepage-related pressure imbalance and the resulting bottom sea water intrusion. Such intrusion dilutes the concentration of methane in the first 50-70 cm of

sediments and effectively prevents methane from leaking to the overlying bottom water. By fitting observed sulfate profiles, our model suggests there has been 1 to 1.8 years of continuous downward flow of bottom seawater at a velocity of 0.3 to 0.6 m/yr. This process provides a short-term negative feedback to the seepage activity of the active pockmarks.

- The results of our steady-state model confirm efficient ~~methane~~ dissolved methane removal through AOM at the active sites. For the three active pockmarks, 29.3 to 40.9 μmol/cm^2/yr of methane is converted to DIC, a regulation of dissolved methane concentration in the sediments for centurial time scale. From the modeling of phosphate profiles, we show that AOM has been persistently active for at last 2-~~3~~ 4 centuries at the three active pockmarks. It is worth noting that, due to the high efficiency of AOM, virtually no dissolved methane escapes from the sediments even at the site where gas hydrate is present below 2 mbsf. AOM may seem to be inefficient because of the documented methane that escapes into the water column. Comparing the efficiency of AOM at removing methane to the amount of methane in the water column is, however, fraught with uncertainty due to assumptions and limitations inherit in the different methods.
- The ultimate sink for methane carbon is the precipitation of authigenic carbonates, the reaction that sequestrates methane over geological time scale. We estimated that 25% to 29% of the methane carbon is ultimately fixed as authigenic carbonates at the active pockmarks.

Acknowledgement

The authors would like to thank the captains, crew members, and scientific parties of both 2008 RSS James Clark Ross cruise and 2013 R/V Helmer Hanssen cruise. This work was supported by the Research Council of Norway through its Centres of Excellence funding scheme, project number 223259. W.G.A. Jr. is now an employee of the US NSF, however any opinion, finding, and conclusions or recommendations expressed in this material are those of W.G.A. Jr. and his coauthors, and do not necessarily reflect the views of the US NSF. We thank Dr. JoLynn Carroll

519 for comments on the earlier version of this manuscript and Joanne Muratori for editorial
520 assistance.

References

Ambrose , W. G. Jr., Panieri, G., Schneider, A., Plaza-Faverola, A., Carroll, M., Åstrøm, K., Locke V, W., and Carroll, J., 2015, Vesicomyid bivalve community indicates prolonged past emission in the Arctic Ocean: (in review).

Baeten, N. J., Laberg, J. S., Vanneste, M., Forsberg, C. F., Kvalstad, T. J., Forwick, M., Vorren, T. O., and Haflidason, H., 2014, Origin of shallow submarine mass movements and their glide planes—Sedimentological and geotechnical analyses from the continental slope off northern Norway: Journal of Geophysical Research: Earth Surface, v. 119, no. 11, p. 2335-2360.

Berndt, C., Feseker, T., Treude, T., Krastel, S., Liebetrau, V., Niemann, H., Bertics, V. J., Dumke, I., Dünnbier, K., Ferré, B., Graves, C., Gross, F., Hissmann, K., Hühnerbach, V., Krause, S., Lieser, K., Schauer, J., and Steinle, L., 2014, Temporal Constraints on Hydrate-Controlled Methane Seepage off Svalbard: Science, v. 343, no. 6168, p. 284-287.

Boetius, A., Ravenschlag, K., Schubert, C. J., Rickert, D., Widdel, F., Gieseke, A., Amann, R., Jorgensen, B. B., Witte, U., and Pfannkuche, O., 2000, A marine microbial consortium apparently mediating anaerobic oxidation of methane: Nature, v. 407, no. 6804, p. 623-626.

Boetius, A., and Wenzhofer, F., 2013, Seafloor oxygen consumption fuelled by methane from cold seeps: Nature Geoscience, v. 6, no. 9, p. 725-734.

Britt, S. L., Bottjer, D. J., Fischer, A. G., Flocks, J. G., and Gorsline, D. S., 1992, X-radiography of horizontal core slabs - a method for greater retrieval of sediment core data: Journal of Sedimentary Petrology, v. 62, no. 4, p. 718-721.

Bünz, S., Polyanov, S., Vadakkepuliyambatta, S., Consolaro, C., and Mienert, J., 2012, Active gas venting through hydrate-bearing sediments on the Vestnesa Ridge, offshore W-Svalbard: Marine Geology, v. 332–334, no. 0, p. 189-197.

Cao, Y., Chen, D., and Cathles, L. M., 2013, A kinetic model for the methane hydrate precipitated from venting gas at cold seep sites at Hydrate Ridge, Cascadia margin, Oregon: Journal of Geophysical Research: Solid Earth, v. 118, no. 9, p. 4669-4681.

Chow, N., Morad, S., and Al-Aasm, I. S., 2000, Origin of authigenic Mn-Fe carbonates and pore-water evolution in marine sediments: evidence from Cenozoic strata of the Arctic Ocean and Norwegian-Greenland Sea (ODP Leg 151): Journal of Sedimentary Research, v. 70, no. 3.

Chuang, P. C., Dale, A. W., Wallmann, K., Haeckel, M., Yang, T. F., Chen, N. C., Chen, H. C., Chen, H. W., Lin, S., Sun, C. H., You, C. F., Horng, C. S., Wang, Y. S., and Chung, S. H., 2013, Relating sulfate and methane dynamics to geology: Accretionary prism offshore SW Taiwan: Geochemistry Geophysics Geosystems, v. 14, no. 7, p. 2523-2545.

Consolaro, C., Rasmussen, T. L., Panieri, G., Mienert, J., Bünz, S., and Sztybor, K., 2014, Carbon isotope ($\delta^{13}C$) excursions suggest times of major methane release during the last 14 ka in Fram Strait, the deep-water gateway to the Arctic: Climate of the Past, v. 10, no. 5, p. 4191-4227.

Crane, K., Sundvor, E., Buck, R., and Martinez, F., 1991, Rifting in the northern Norwegian-Greenland Sea: Thermal tests of asymmetric spreading: Journal of Geophysical Research: Solid Earth (1978–2012), v. 96, no. B9, p. 14529-14550.

Eiken, O., and Hinz, K., 1993, Contourites in the Fram Strait: Sedimentary Geology, v. 82, no. 1, p. 15-32.

Engen, Ø., Faleide, J. I., and Dyreng, T. K., 2008, Opening of the Fram Strait gateway: a review

Formatted: Font: (Default) Times New Roman, 12 pt

Formatted: Font: (Default) Times New Roman, 12 pt

of plate tectonic constraints: Tectonophysics, v. 450, no. 1, p. 51-69.
Greinert, J., Veloso, M., De Batist, M. A., and Mienert, J., Hydroacoustic quantification of free-gas venting offshore Svalbard, Arctic: Changes in space and time, *in* Proceedings AGU Fall Meeting Abstracts2013, Volume 1, p. 07.
Haeckel, M., Boudreau, B. P., and Wallmann, K., 2007, Bubble-induced porewater mixing: A 3-D model for deep porewater irrigation: Geochimica Et Cosmochimica Acta, v. 71, no. 21, p. 5135-5154.
Haeckel, M., Suess, E., Wallmann, K., and Rickert, D., 2004, Rising methane gas bubbles form massive hydrate layers at the seafloor: Geochimica et Cosmochimica Acta, v. 68, no. 21, p. 4335-4345.
Hensen, C., Zabel, M., Pfeifer, K., Schwenk, T., Kasten, S., Riedinger, N., Schulz, H. D., and Boettius, A., 2003, Control of sulfate pore-water profiles by sedimentary events and the significance of anaerobic oxidation of methane for the burial of sulfur in marine sediments: Geochimica et Cosmochimica Acta, v. 67, no. 14, p. 2631-2647.
Hinrichs, K. U., and Boetius, A., 2003, The anaerobic oxidation of methane: new insights in microbial ecology and biogeochemistry, *in* Wefer, G., Billett, D., Hebbeln, D., Jorgensen, B., Schluter, M., and van Weering, T., eds., Ocean Margin Systems: Verlag Berlin Heidelberg Germany, Springer, p. 457-477.
Holstein, J. M., and Wirtz, K. W., 2010, Organic matter accumulation and degradation in subsurface coastal sediments: a model-based comparison of rapid sedimentation and aquifer transport: Biogeosciences, v. 7, no. 11, p. 3741-3753.
Hong, W.-L., Solomon, E. A., and Torres, M. E., 2014a, A kinetic-model approach to quantify the effect of mass transport deposits on pore water profiles in the Krishna–Godavari Basin, Bay of Bengal: Marine and Petroleum Geology, v. 58, p. 223-232.
Hong, W.-L., Torres, M. E., Kim, J.-H., Choi, J., and Bahk, J.-J., 2014b, Towards quantifying the reaction network around the sulfate–methane-transition-zone in the Ulleung Basin, East Sea, with a kinetic modeling approach: Geochimica et Cosmochimica Acta, v. 140, no. 1, p. 127-141.
Hovland, M., Gardner, J. V., and Judd, A. G., 2002, The significance of pockmarks to understanding fluid flow processes and geohazards: Geofluids, v. 2, no. 2, p. 127-136.
Hovland, M., and Judd, A. G., 1992, The global production of methane from shallow submarine sources: Continental Shelf Research, v. 12, no. 10, p. 1231-1238.
Howe, J. A., Shimmield, T. M., Harland, R., and Eyles, N., 2008, Late Quaternary contourites and glaciomarine sedimentation in the Fram Strait: Sedimentology, v. 55, no. 1, p. 179-200.
Hustoft, S., Bünz, S., Mienert, J., and Chand, S., 2009, Gas hydrate reservoir and active methane-venting province in sediments on< 20 Ma young oceanic crust in the Fram Strait, offshore NW-Svalbard: Earth and Planetary Science Letters, v. 284, no. 1, p. 12-24.
Johnson, J. E., Mienert, J., Plaza-Faverola, A., Vadakkepuliyambatta, S., Knies, J., Bünz, S., Andreassen, K., and Ferré, B., 2015, Abiotic methane from ultraslow-spreading ridges can charge Arctic gas hydrates: Geology, v. 43, no. 5, p. 371-374.
Jourabchi, P., Van Cappellen, P., and Regnier, P., 2005, Quantitative interpretation of pH distributions in aquatic sediments: a reaction-transport modeling approach: American Journal of Science, v. 305, no. 9, p. 919-956.
Judd, A. G., Hovland, M., Dimitrov, L. I., Garcia-Gil, S., and Jukes, V., 2002, The geological methane budget at Continental Margins and its influence on climate change: Geofluids, v. 2, no. 2, p. 109-126.

Formatted: Font: (Default) Times New Roman, 12 pt

Knittel, K., and Boetius, A., 2009, Anaerobic oxidation of methane: progress with an unknown process: Annual review of microbiology, v. 63, p. 311-334.
Krylova, E. M., and Sahling, H., 2010, Vesicomyidae (Bivalvia): current taxonomy and distribution: PLoS One, v. 5, no. 4, p. e9957.
Liu, X. L., and Flemings, P. B., 2006, Passing gas through the hydrate stability zone at southern Hydrate Ridge, offshore Oregon: Earth And Planetary Science Letters, v. 241, no. 1-2, p. 211-226.
Löwemark, L., and Werner, F., 2001, Dating errors in high-resolution stratigraphy: a detailed X-ray radiograph and AMS-14 C study of Zoophycos burrows: Marine Geology, v. 177, no. 3, p. 191-198.
Luff, R., Greinert, J., Wallmann, K., Klaucke, I., and Suess, E., 2005, Simulation of long-term feedbacks from authigenic carbonate crust formation at cold vent sites: Chemical Geology, v. 216, no. 1-2, p. 157-174.
Luff, R., Haeckel, M., and Wallmann, K., 2001, Robust and fast FORTRAN and MATLAB (R) libraries to calculate pH distributions in marine systems: Computers & Geosciences, v. 27, no. 2, p. 157-169.
Luff, R., and Wallmann, K., 2003, Fluid flow, methane fluxes, carbonate precipitation and biogeochemical turnover in gas hydrate-bearing sediments at Hydrate Ridge, Cascadia Margin: Numerical modeling and mass balances: Geochimica Et Cosmochimica Acta, v. 67, no. 18, p. 3403-3421.
MacDonald, I., Guinasso, N., Sassen, R., Brooks, J., Lee, L., and Scott, K., 1994, Gas hydrate that breaches the sea floor on the continental slope of the Gulf of Mexico: Geology, v. 22, no. 8, p. 699-702.
Murphy, J., and Riley, J. P., 1962, A modified single solution method for the determination of phosphate in natural waters: Analytica chimica acta, v. 27, p. 31-36.
Mörz, T., Karlik, E. A., Kreiter, S., and Kopf, A., 2007, An experimental setup for fluid venting in unconsolidated sediments: New insights to fluid mechanics and structures: Sedimentary Geology, v. 196, no. 1-4, p. 251-267.
Nedoncelle, K., Lartaud, F., De Rafelis, M., Boulila, S., and Le Bris, N., 2013, A new method for high-resolution bivalve growth rate studies in hydrothermal environments: Marine biology, v. 160, no. 6, p. 1427-1439.
Nikolovska, A., Sahling, H., and Bohrmann, G., 2008, Hydroacoustic methodology for detection, localization, and quantification of gas bubbles rising from the seafloor at gas seeps from the eastern Black Sea: Geochemistry, Geophysics, Geosystems, v. 9, no. 10.
O'Brien, N. R., 1987, The effects of bioturbation on the fabric of shale: Journal of Sedimentary Research, v. 57, no. 3.
Panieri, G., James, R. H., Camerlenghi, A., Westbrook, G. K., Consolaro, C., Cacho, I., Cesari, V., and Cervera, C. S., 2014, Record of methane emissions from the West Svalbard continental margin during the last 23.500 yrs revealed by $\delta^{13}C$ of benthic foraminifera: Global and Planetary Change, v. 122, p. 151-160.
Petersen, C. J., Bünz, S., Hustoft, S., Mienert, J., and Klaeschen, D., 2010, High-resolution P-Cable 3D seismic imaging of gas chimney structures in gas hydrated sediments of an Arctic sediment drift: Marine and Petroleum Geology, v. 27, no. 9, p. 1981-1994.
Plaza-Faverola, A., Bünz, S., Johnson, J. E., Chand, S., Knies, J., Mienert, J., and Franek, P., 2015, Role of tectonic stress in seepage evolution along the gas hydrate-charged Vestnesa Ridge, Fram Strait: Geophysical Research Letters, v. 42, no. 3, p. 2014GL062474.
Rebesco, M., Wåhlin, A., Laberg, J. S., Schauer, U., Beszczynska-Möller, A., Lucchi, R. G.,

Formatted: Font: (Default) Times New Roman, 12 pt

Noormets, R., Accettella, D., Zarayskaya, Y., and Diviacco, P., 2013, Quaternary contourite drifts of the Western Spitsbergen margin: Deep Sea Research Part I: Oceanographic Research Papers, v. 79, no. 0, p. 156-168.

Regnier, P., Dale, A. W., Arndt, S., LaRowe, D. E., Mogollon, J., and Van Cappellen, P., 2011, Quantitative analysis of anaerobic oxidation of methane (AOM) in marine sediments: A modeling perspective: Earth-Science Reviews, v. 106, no. 1-2, p. 105-130.

Sahling, H., Römer, M., Pape, T., Bergès, B., dos Santos Fereirra, C., Boelmann, J., Geprägs, P., Tomczyk, M., Nowald, N., and Dimmler, W., 2014, Gas emissions at the continental margin west off Svalbard: mapping, sampling, and quantification: Biogeosciences Discussions, v. 11, p. 7189-7234.

Schöne, B. R., and Giere, O., 2005, Growth increments and stable isotope variation in shells of the deep-sea hydrothermal vent bivalve mollusk Bathymodiolus brevior from the North Fiji Basin, Pacific Ocean: Deep Sea Research Part I: Oceanographic Research Papers, v. 52, no. 10, p. 1896-1910.

Smith, A. J., Mienert, J., Bunz, S., and Greinert, J., 2014, Thermogenic methane injection via bubble transport into the upper Arctic Ocean from the hydrate-charged Vestnesa Ridge, Svalbard: Geochemistry Geophysics Geosystems, v. 15, no. 5, p. 1945-1959.

Snyder, G. T., Hiruta, A., Matsurnoto, R., Dickens, G. R., Tomaru, H., Takeuchi, R., Komatsubara, J., Ishida, Y., and Yu, H., 2007, Pore water profiles and authigenic mineralization in shallow marine sediments above the methane-charged system on Umitaka Spur, Japan Sea: Deep-Sea Research Part Ii-Topical Studies in Oceanography, v. 54, no. 11-13, p. 1216-1239.

Solomon, E. A., Kastner, M., Jannasch, H., Robertson, G., and Weinstein, Y., 2008, Dynamic fluid flow and chemical fluxes associated with a seafloor gas hydrate deposit on the northern Gulf of Mexico slope: Earth and Planetary Science Letters, v. 270, no. 1, p. 95-105.

Sommer, S., Pfannkuche, O., Linke, P., Luff, R., Greinert, J., Drews, M., Gubsch, S., Pieper, M., Poser, M., and Viergutz, T., 2006, Efficiency of the benthic filter: Biological control of the emission of dissolved methane from sediments containing shallow gas hydrates at Hydrate Ridge: Global Biogeochemical Cycles, v. 20, no. 2, p. GB2019.

Steefel, C. I., 2009, CrunchFlow- Software for Modeling Multicomponent Reactive Flow and Transport: User's Manual.

Sun, X., and Turchyn, A. V., 2014, Significant contribution of authigenic carbonate to marine carbon burial: Nature Geoscience, v. 7, no. 3, p. 201-204.

Tamelander, T., Aubert, A. B., and Riser, C. W., 2012, Export stoichiometry and contribution of copepod faecal pellets to vertical flux of particulate organic carbon, nitrogen and phosphorus: Marine Ecology Progress Series, v. 459, p. 17-28.

Torres, M. E., Wallmann, K., Trehu, A. M., Bohrmann, G., Borowski, W. S., and Tomaru, H., 2004, Gas hydrate growth, methane transport, and chloride enrichment at the southern summit of Hydrate Ridge, Cascadia margin off Oregon: Earth and Planetary Science Letters, v. 226, no. 1-2, p. 225-241.

Treude, T., Boetius, A., Knittel, K., Wallmann, K., and Jorgensen, B. B., 2003, Anaerobic oxidation of methane above gas hydrates at Hydrate Ridge, NE Pacific Ocean: Marine Ecology-Progress Series, v. 264, p. 1-14.

Trotsyuk, V. Y., and Avilov, V., 1988, Disseminated flux of hydrocarbon gases from the sea bottom and a method of measuring it, *in* Proceedings Doklady Earth Science, Volume 291, p. 218-220.

Formatted: Font: (Default) Times New Roman, 12 pt

Tryon, M. D., Brown, K. M., Torres, M. E., Trehu, A. M., McManus, J., and Collier, R. W., 1999, Measurements of transience and downward fluid flow near episodic methane gas vents, Hydrate Ridge, Cascadia: Geology, v. 27, no. 12, p. 1075-1078.

Tryon, M. D., Brown, K. M., and Torres, M. E., 2002, Fluid and chemical flux in and out of sediments hosting methane hydrate deposits on Hydrate Ridge, OR, II: Hydrological processes: Earth And Planetary Science Letters, v. 201, no. 3-4, p. 541-557.

Tryon, M. D., Henry, P., and Hilton, D. R., 2012, Quantifying submarine fluid seep activity along the North Anatolian Fault Zone in the Sea of Marmara: Marine Geology, v. 315, p. 15-28.

Van Daele, M., Cnudde, V., Duyck, P., Pino, M., Urrutia, R., and De Batist, M., 2014, Multidirectional, synchronously-triggered seismo-turbidites and debrites revealed by X-ray computed tomography (CT): Sedimentology, v. 61, no. 4, p. 861-880.

Veloso, M., Greinert, J., Mienert, J., and De Batist, M., 2015, A new methodology for quantifying bubble flow rates in deep water using splitbeam echosounders: Examples from the Arctic offshore NW-Svalbard: Limnology and Oceanography: Methods, v. 13, no. 6, p. 267-287.

Veloso, M., Mienert, J., De Batist, M., and Greinert, J., Methane flux estimation of a large seep area offshore Svalbard based on visual observations and inverse hydroacoustic modeling, *in* Proceedings EGU General Assembly Conference Abstracts2014, Volume 16, p. 13130.

von Rad, U., Rösch, H., Berner, U., Geyh, M., Marchig, V., and Schulz, H., 1996, Authigenic carbonates derived from oxidized methane vented from the Makran accretionary prism off Pakistan: Marine Geology, v. 136, no. 1, p. 55-77.

Wallmann, K., Aloisi, G., Haeckel, M., Obzhirov, A., Pavlova, G., and Tishchenko, P., 2006a, Kinetics of organic matter degradation, microbial methane generation, and gas hydrate formation in anoxic marine sediments: Geochimica et Cosmochimica Acta, v. 70, no. 15, p. 3905-3927.

Wallmann, K., Drews, M., Aloisi, G., and Bohrmann, G., 2006b, Methane discharge into the Black Sea and the global ocean via fluid flow through submarine mud volcanoes: Earth and Planetary Science Letters, v. 248, no. 1-2, p. 545-560.

Westbrook, G. K., Thatcher, K. E., Rohling, E. J., Piotrowski, A. M., Paelike, H., Osborne, A. H., Nisbet, E. G., Minshull, T. A., Lanoiselle, M., James, R. H., Huehnerbach, V., Green, D., Fisher, R. E., Crocker, A. J., Chabert, A., Bolton, C., Beszczynska-Moeller, A., Berndt, C., and Aquilina, A., 2009, Escape of methane gas from the seabed along the West Spitsbergen continental margin: Geophysical Research Letters, v. 36.

Zabel, M., and Schulz, H. D., 2001, Importance of submarine landslides for non-steady state conditions in pore water systems - lower Zaire (Congo) deep-sea fan: Marine Geology, v. 176, no. 1-4, p. 87-99.

Figure Captions

Figure 1: Geographic location and the chimney system of our study sites. (A) Map showing the regional bathymetry and the location of Vestnesa Ridge. (B) Detail bathymetry of E. Vestnesa Ridge and the location of the five study sites. (C) Seismic profile crossing one of the active pockmarks investigated showing a well-established chimney system beneath.

Figure 2: Profiles of key pore water species and results from the steady-state modeling. Our model estimates the rate of key reactions (as shown by the red dash lines) by fitting the measured pore water profiles (blue and green solid lines). The discrepancy between the observed and modeled profiles (the first 50-70 cm at the three active sites) is due to a short-term (< years) non-steady-state behavior of the system which is not considered by our steady-state model.

Figure 3: X-radiograph and visual description of cores from ~~four of the study sites~~HH13-197, -199, -200, and -203. We did not observe any anomalous sedimentary feature that could be associated with any geological events (*e.g.,* slope failures, mass transport events), bioturbation and gas tubes.

Figure 4: (A&B) Illustration of the aqueous pump mechanism. (C) - (E) Simulation results of sulfate profiles for the downward fluid water on the three active sites. Red solid lines show the initial condition used in this simulation. Green solid lines show the best fit model results. Our model is only able to constrain the longest time (*Dt*) and smallest *Darcy* flux (*q*) required, as shown on the figures.

Figure 5: Model estimated phosphate concentration by POSCR for different length of time and the comparison with the observed profiles.

775 Figure 6: Comparison of AOM rates derived from our steady-state model with the global dataset
776 compiled by Regnier et al. (2011). We estimated the theoretical maximum AOM rate by
777 extrapolating our estimation from 4 sites to the point where the depth of SMTZ is 2 cm, the
778 shallowest SMTZ ever reported in the literatures (Treude et al., 2003; Wallmann et al., 2006b).

779

780 Figure 7: Schematic summary of the three methane removal processes and reactions we model.
781 The importance of these processes/reactions is a function of their proximity to the center of
782 pockmark as well as the time scale over which they operate.

783